PHOTOCATALYTIC HYDROGEN PRODUCTION USING STRONTIUM TITANATE AND SUPPORTED SILVER NANOPARTICLES

by

SEAN TAYLOR

A thesis submitted to the

Graduate School-Camden

Rutgers, The State University of New Jersey

in partial fulfillment of the requirements

for the degree of Master of Science

Graduate Program in Chemistry

written under the direction of

Dr. Alexander Samokhvalov

and approved by

_____

Dr. Alexander Samokhvalov

_____

Dr. Alex J. Roche

_____

Dr. George Kumi

Camden, New Jersey

May 2016

THESIS ABSTRACT

Photocatalytic Hydrogen Production Using Strontium Titanate and Supported Silver Nanoparticles

By SEAN TAYLOR

Thesis Director:

Dr. Alexander Samokhvalov

Semiconductors have been gaining interest in the field of photocatalysis due to their ability to efficiently harvest energy from light, their versatility in performing many different photocatalytic reactions, and for making electronic devices. Plasmonic metal nanoparticles have also been increasingly studied for their use in applications from spectroscopic enhancement and bioanalytics to photocatalysis. In this study we photochemically deposited silver metal nanoparticles onto the surface of strontium titanate in-situ using silver nitrate and investigated how they affect the photocatalytic production of hydrogen from glycerol and water at several silver loadings. The photocatalytic activity of the silver doped photocatalysts was also studied at different spectral regions of light. We have confirmed the presence of silver nanoparticles using UV-Vis Diffuse Reflectance.

Furthermore it was found that the photocatalytic ability of the silver doped photocatalysts had a nonlinear dependence on the amount of silver loading. There were two maxima of the photocatalytic ability which we propose was due to the creation of plasmonic nanoparticles and the overloading of silver on the strontium titanate which would inhibit light absorption of the bulk photocatalyst.

We also studied the kinetics of silver deposition onto the strontium titanate using Photoluminescence spectroscopy. This is due to the strontium titanate first photocatalytically reducing the silver ions into the metallic nanoparticles.

Acknowledgments and Dedication

I would like to thank Dr. Alexander Samokhvalov, who was my M.S. thesis advisor, for his continuous guidance and support throughout this thesis, for supervising my research and helping me grow intellectually. I would like to thank my M.S. Committee members Dr. Alex J. Roche and Dr. George Kumi for their advice on my research and their help in reviewing my thesis. I would also like to thank the faculty and staff of the Chemistry Department for all of their guidance and education they have given me during my studies at Rutgers University Camden Campus. I would like to express my extreme gratitude to my family who has supported me all through my life and given me the strength and encouragement when I needed it most.

Table of Contents

List of Figures

List of Tables

1 Introduction

1.1 Semiconductors

Semiconductors are increasingly being studied and widely used for their electronic and catalytic abilities. Semiconductors have even been used in the field of electronics as structures for transparent electronics [1]. Recently transition metal semiconductors are being studied for use in the field of photocatalysis due to (1) their ability to absorb various wavelengths of electromagnetic radiation and (2) their ability to use that absorbed energy to promote reduction-oxidation catalysis [2]. The interest in the use of these inorganic semiconductors is also amplified by the fact that they are stable to many harsh conditions, such as pH, air, and other chemical reducing and oxidizing agents [3]. The ability to withstand these conditions allows for application in many different fields of study. However, for many of these applications more understanding of fundamental processes is required.

Semiconductors are materials that have an energy gap between the valence and conduction bands. Inorganic semiconductors can be composed of metal oxides, metal sulfides, and various combinations of different elements as well [2-5]. These semiconductors have different crystalline lattice structures such as orthorhombic, cubic, and tetragonal. The different band gaps correspond to different wavelengths of light they are able to absorb. This is of great importance to photocatalysis. Surface area plays a role in photocatalysis since all of the chemistry happens on or near the surface of the photocatalyst [6]. A major issue with the use of inorganic metal oxide photocatalysts is that the band gap is too large and requires a great amount of energy in order to excite an electron from the valence band to the conduction band; thus only making them useful for

UV photocatalysis. The mechanism for photocatalysis using metal oxide semiconductors is shown in Figure 1. The aim of this and other research projects is to close that gap to make it more suitable for photocatalysis at lower photon energy levels.

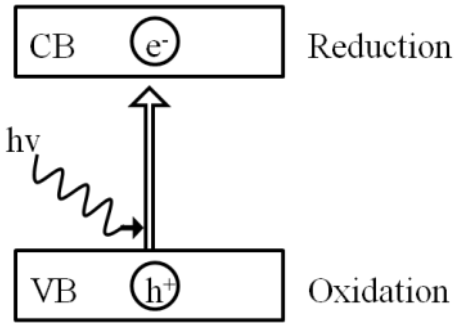

Figure 1: General mechanism of semiconductor photocatalysis.

1.2 Semiconductor Photocatalysis

Converting solar to chemical energy by photocatalysis has been quickly gaining interest in recent years. A major portion of these studies is in the field of semiconductors. Transition metal semiconductors come in a variety of forms each having different conduction and valence band energy levels, most of which only absorb in the UV region [3]. Metal oxide and sulfide semiconductors are used for photocatalysis by utilizing the conduction and valence band levels. When a semiconductor photocatalyst is exposed to light of a certain energy an electron is excited from the low energy (valence) band to the higher energy (conduction) band leaving a hole in the valence band as shown in Figure 1. The energy difference between the valence band and the conduction band is called the band gap. Once the semiconductor is in the excited state, the excited electron and the hole perform the reduction and oxidation respectively [3]. The process for water splitting using a semiconductor photocatalyst is shown in Figure 2. In recent years semiconductor

photocatalysts have been used for the decomposition of organic pollutants in water into CO_2 and H_2O [2], organic dye decompositions [7], and epoxidation reactions [8].

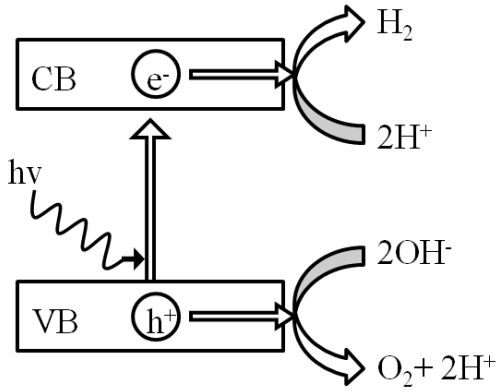

Figure 2: Mechanism for water splitting using a semiconductor photocatalyst.

1.3 Photocatalysis with Metal-doped Semiconductors

Doped photocatalysts are a class of semiconductor photocatalysts that have been impregnated with a different atom into their structure or crystal lattice [9]. Many different metal dopants such as Zn [5], Cr, Mn, Ir, Sb, Ru, and Rh [10] have been reported to increase the photocatalytic activity of semiconductors by reducing the band gap energy to a level suitable for absorbing visible light. The metal dopants introduce new energy levels within the photocatalyst that can either be an electron donor or electron acceptor level depending on the type of dopant used [11]. The mechanism for this type of photocatalysis is shown in Figure 3. These new levels in essence decrease the energy gap and allow for the absorption of lower energy light promoting visible light catalysis.

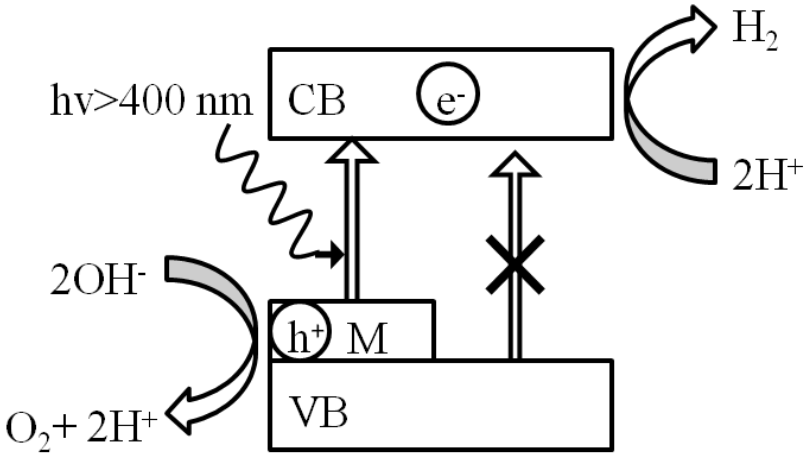

Figure 3: Mechanism for photocatalytic water splitting using a metal doped semiconductor.

Another common way to dope photocatalysts is to deposit metals directly onto the surface of the catalyst. It is well known that platinum deposited onto the surface of a semiconductor will greatly enhance its photocatalytic activity especially in producing hydrogen [12]. It has been reported that depositing platinum onto the surface of $SrTiO_3$ enhanced its catalytic ability by 400 percent [13]. The effects of depositing other metals such as gold, palladium, copper, rhodium, and nickel onto the surface of different semiconductor photocatalysts has also greatly increased their performance [14].

One way that the metal nanoparticles help to promote photocatalysis is through a phenomenon known as Surface Plasmon Resonance (SPR). Linic et al. states "SPR can be described as the resonant photon-induced collective oscillation of valence electrons, established when the frequency of photons matches the natural frequency of surface electrons oscillating against the restoring force of positive nuclei" [15]. When the nanoparticles are irradiated with wavelengths that match that resonant frequency they can

eject an electron out of their electron cloud and into the semiconductor which is known as photoinjection [16] (Figure 4). The metal nanoparticles need to be small (below 20 nm) so that upon excitation the electrons can break free from the electron cloud [16]. The interaction between the metal nanoparticles and the semiconductor causes a shift in the Fermi level of the system. This is due to the Fermi level of the noble metal nanoparticles being around 0eV on the NHE scale which is optimal for water splitting and other catalytic reactions [15].

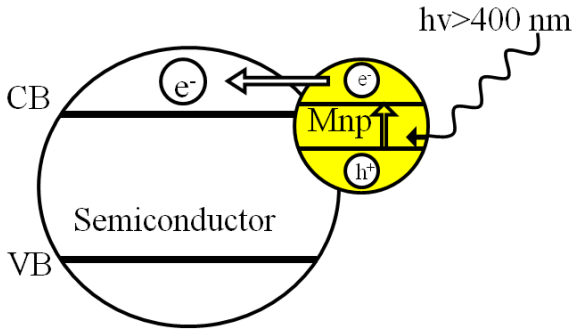

Figure 4: Mechanism of photoinjection of an electron from the metal nanoparticle into the conduction band of the semiconductor.

1.4 Alkaline Earth Metal Titanates

Alkaline earth metal titanates are a group of semiconductors with the formula $XTiO_3$ where X is an alkaline earth metal such as calcium, barium, or strontium. These materials usually have wide band gaps around 3 eV or higher [11]. Alkaline earth metal titanates have been studied for many years for their different physical and electrochemical properties. They have similar electronic properties with the conduction band arising from the degenerated Ti 3d-t_{2g} orbital [17]. Besides photocatalysis, these

materials have found uses in electronic devices in the form of thin film transistors and resistors [1] and electroceramics [18]. Although there are others [4,5,19], the most common method for synthesis is by the sol-gel procedure [18] which involves dissolving the reactants then drying and subsequently calcining the powders.

1.5 Photocatalysis with Alkaline Earth Metal Titanates

Alkaline earth metal titanates have been used for different applications and photocatalytic reactions. Due to their band gap energy they have been widely used for UV photocatalysis but not often for hydrogen generation. Studies have been conducted where alkaline earth metal titanates have been used for photocatalytically promoting organic reactions such as ethylene epoxidation and propene oxidation [20,21]. A major portion of the research being conducted on these catalysts is aimed at the photocatalytic cleaning of waste water. These projects often study the ability to decompose organic molecules that are the pollutants released during various industrial processes [22]. Textile industries are a major culprit of accidentally releasing dyes into the environment. The use of these photocatalysts for dye decomposition has been the topic of many studies [7,23,24]. These studies have gathered valuable information on the effectiveness of this group of photocatalysts but much has yet to be learned about the mechanistic pathways which drive these reactions.

In order for a semiconductor to be a good photocatalyst for water splitting it must satisfy several criteria. In order to be able to perform the photocatalytic splitting of water into hydrogen and oxygen it must have a conduction band level more negative than that of the hydrogen reduction level and a valence band level more positive than the water

oxidation level [14]. The water reduction potential is 0 eV (with respect to the normal hydrogen electrode) and the oxidation potential is 1.23 eV making the energy gap correspond to around 1000 nm [3]. The ideal photocatalyst for water splitting that would use the energy in the visible light region would have a valence band level more negative than 3.0 eV and a conduction band slightly more negative than 0 eV making it absorb from 400 nm to slightly above 1000 nm which encompasses around 50% of the solar energy [14].

This requirement has greatly hindered the use of many semiconductor photocatalysts. Many of the transition metal oxide semiconductors have transition metal cations with d^0 or d^{10} electronic configurations and O2p orbitals making the valence and conduction bands respectively [25]. The O2p orbitals are usually about +3 eV or more positive making the band gap too large to absorb visible light [25]. This makes the majority of semiconductor photocatalysts only active in the UV region of the spectrum. Stability becomes a concern when attempting to use semiconductor photocatalysts at an industrial scale. Some catalysts will undergo photo self corrosion and decompose after a short time such as CdS [26]. In general sulfide semiconductors are unstable and undergo photoanodoic corrosion while most oxides are more stable over time [24].

In this work the semiconductor photocatalyst used is strontium titanate ($SrTiO_3$) nanopowder. Strontium titanate has a white appearance and is optically transparent in the visible range [27]. It has a cubic perovskite crystal structure at room temperature as in Supplementary Figure 1**,** but has a phase transition into a tetragonal phase at 108 K [27]. The reported surface area for commercial strontium titanate nanopowder is between 28 m^2/g and 32 m^2/g [6]. The band gap for $SrTiO_3$ has been determined to be 3.2 eV [28].

This is often used for UV photocatalysis since it corresponds to an absorption wavelength of 387 nm. Table 1 shows some rates obtained for pure strontium titanate. There have been studies in which strontium titanate was doped with another metal ion in its crystal lattice as well as had metal nanoparticles deposited on its surface. Tables 2 and 3 show the rates obtained from doping in the lattice as well as with surface-loaded metal nanoparticles. Since Pyrex glass has an absorption spectrum in the UV range, it is worth noting when a Pyrex reaction vessel is used since it alters the intensity of light reaching the reaction mixture. When a Pyrex reaction vessel was used in the experiments listed in the tables, "Pyrex" is written in the "Light source" column.

Figure S1: Cubic structure of strontium titanate at room temperature. Large green spheres are Sr, middle blue sphere is Ti, small red spheres are O

Table 1: Previously reported rates of hydrogen production from pure $SrTiO_3$

$SrTiO_3$ State	Light source	Conditions	Activity μmol/hg	Ref.
Nanocrystaline	300 W Xe Pyrex >415 nm	MeOH	0	[4]
Nanocrystaline	2816 W Hg Pyrex	MeOH	46	[6]
Mesoporous	2816 W Hg Pyrex	MeOH	156	[6]
Mesoporous	300 W Xe Pyrex >400 nm	DEA donor	13.9	[13]
Nanocrystaline	400 W Hg	10 wt% MeOH	225	[19]
Nanocrystaline	300 W Xe Pyrex >420 nm	20% MeOH	0	[29]

Table 2: Rates of hydrogen production from metal promoted $SrTiO_3$

Form of STO	Promoter	Donor	Light source	Rate μmol/hg	Ref.
$SrTiO_3$:Na			400 W Hg Pyrex<400 nm	22220	[3]
$SrTiO_3$:Ta	Rh $Cr_{2-x}O_3$		450 W Hg Pyrex>400 nm	14160	[3]
$SrTiO_3$:La	CoO_x	Na_2CO_3	400 W Xe <400 nm	2800	[3]
$SrTiO_3$:Rh/Ta	Rh and Ta	MeOH	300 W Xe Pyrex >415 nm	2130	[4]
$SrTiO_3$	TiO_2	Propanol	150 W Hg Pyrex<400 nm	150	[12]
$SrTiO_3$	Rh	10 wt% MeOH	400 W Hg	1115	[19]
composite	NiO		Xe 400 W 250-380 nm	28	[30]
Meso $SrTiO_3$	Au	Formic acid	176 W Hg Pyrex <400 nm	647	[31]

Table 3: Rates of hydrogen production from Metal nanoparticle promoted $SrTiO_3$

Metal NP	Donor	Light source	Rate μmol/hg	Ref.
Pt	30 vol% MeOH	High pressure Hg 500 W λ≥210 nm	76000	[32]
Pt	30 vol% MeOH	High pressure Hg 500 W λ≥420 nm	0	[32]
Pt	20 vol% MeOH	300 W Xe >400 nm	95	[33]
Rh	20 vol% MeOH	300 W Xe>400 nm	45	[33]
Cu	60 vol% MeOH	300 W high pressure Hg	3292	[34]

Metal nanoparticles have gained interest due to their unconventional properties that the bulk metals do not display such as SPR. The ability to perform SPR and photoinjection is dependent on several criteria. The size and shape of the metal nanoparticle has a great effect on the strength and frequencies at which the SPR occurs. Metal nanoparticles usually have broad absorption spectra with extremely large molar extinction coefficients over both UV and visible light regions which is useful when attempting to increase photocatalytic activity into the visible region [35]. It has been shown that for silver nanoparticles the absorption spectra greatly depend on the shape of the particle, namely wires, spheres, or cubes, as well as the size (which red shifts the

absorption maxima with increasing size) [15]. The dependence on size and shape allows for the ability to tune the properties of the nanoparticles. A recent study showed that for silver nanoparticles the absorption peak maxima can be tuned from 400 nm to 1000 nm using nanosphere lithography [36].

1.6 Silver Deposition

Several methods of depositing metal nanoparticles onto the surface of semiconductor photocatalysts have been studied and performed. The method of deposition is very important to the photocatalytic and plasmonic properties of the metal nanoparticles since different methods produce different shapes and sizes of the nanoparticles. One prevalent method is photo-reduction of metal ions in solution. Primarily metal salts, such as nitrates, are dissolved in water or a water solution along with the catalyst then exposed to light causing the reduction of the metal ions. After the deposition of the nanoparticles the photocatalysts are usually washed, dried, and calcined for various amounts of time [37-41]. Another common method for silver deposition is the use of the incipient wetness impregnation method [8,20]. This method is based upon the ability of the semiconductors to absorb the metal ions into their pores. This is done by mixing or submerging the semiconductor substrate in a metal salt or complex solution and waiting a certain amount of time then washing the excess solution away followed by drying and calcination. There has also been a study where silver nanoparticles were synthesized using microwave dielectric heating [42]. Each of these methods requires that the metal nanoparticle catalyst be prepared outside of the reaction vessel adding more steps to the synthesis and more opportunities for contamination and oxidation.

In this work we have used a “one-pot” in-situ method. This method removes the some sources of contamination and oxidation that are inherent in the other methods, as well as makes for an easier preparation and application of the photocatalysts. By removing the drying and calcining processes the catalysts are not exposed to air which could reoxidize the metal nanoparticles thus destroying their catalytic ability. Synthesizing the catalyst within the reaction vessel will also benefit the industrial application of this system since it removes the equipment necessary for the washing, drying, etc. of the catalyst. We have used the photocatalytic reduction of silver from silver nitrate solutions in-situ to create the silver nanoparticles on the surface of the strontium titanate in which the strontium titanate would photocatalytically reduce the silver ions into silver metal as previously reported for other metal oxides [43,44].

1.7 Photocatalytic Enhancement by Supported Silver Nanoparticles

Two mechanisms in which the metal nanoparticles enhance the photocatalytic ability of the semiconductor photocatalysts have been proposed. The first method applies more in the UV excitation of the semiconductor itself. When an electron in the valence band of the semiconductor is excited with UV light to the conduction band it creates a positive hole in the valence band. These photogenerated electron-hole pairs can be easily recombined which limits the effectiveness and efficiency of the catalysts [30]. In the first proposed mechanism the photoexcited electron would move from the semiconductor’s conduction band into the metal nanoparticle [40] shown in Figure 5. This happens at the interface between the metal nanoparticles and the surface of the semiconductor. This contact can give rise to a Schottky barrier which makes the metal nanoparticle act as an electron trap delaying the electron from recombining with its hole [45]. This allows for

the hole to more efficiently interact with the target species promoting oxidation. The electron trapped on the metal nanoparticle can then be used for the reduction half reaction.

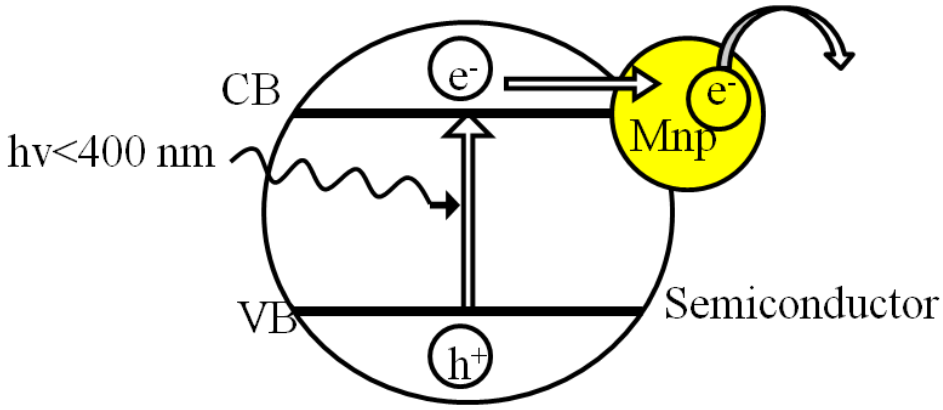

Figure 5: Mechanism of charge trapping due to a metal nanoparticle.

The second mechanism considers the effects of visible light on the catalytic system. Upon excitation of the metal nanoparticle's plasmon resonance, an electron is injected from the nanoparticle into the valence band of the semiconductor via the previously mentioned photoinjection. Instead of an electron being excited from the valence band of the semiconductor an electron is photoinjected from the metal into the conduction band of the semiconductor [28]. This causes the hole to be present on the metal nanoparticle which is beneficial since it is on the surface of the catalyst and not in the bulk like in the excitation of the semiconductor itself has. The scheme of this mechanism is shown in Figure 4.

1.8 Sacrificial Donors

There have been several studies which investigate the production of hydrogen and other photocatalytic reactions using a sacrificial electron donor. The purpose of a

sacrificial electron donor is to be more easily oxidized by the electron hole in the valence band of the semiconductor catalysts than the water or other target molecule [46]. This effect helps to increase the lifetime of the conduction band electron allowing for more time to react and consequently the higher efficiency of the catalyst [41]. Many studies have included sacrificial donors that are organic molecules that usually contain at least one –OH group such as alcohols and carboxylic acids. The most common donors include methanol, acetic acid, ethanol, and sodium carbonate [3]. Many organic pollutants can be used as sacrificial donors which makes this type of photocatalysis beneficial with not only producing hydrogen but also removing pollutants from waste water. The sacrificial electron donors upon being oxidized can eventually be broken down and produce CO_2 as a byproduct. Figure 6 shows a generic scheme of the mechanism of electron donation by a sacrificial electron donor.

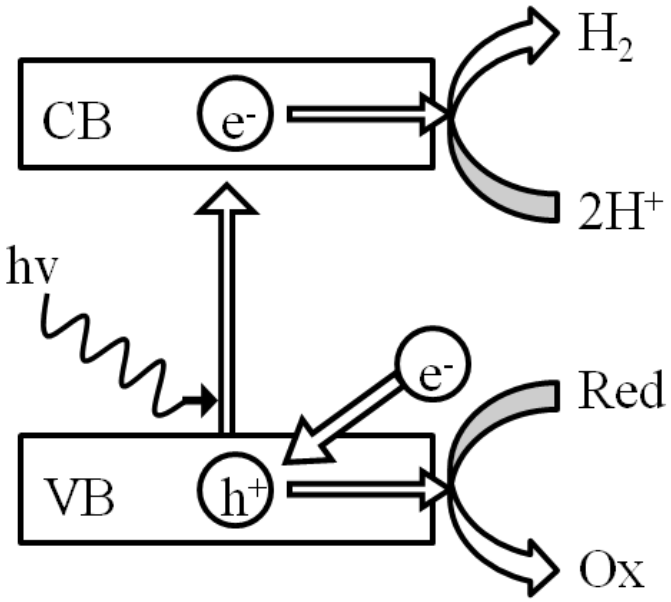

Figure 6: Mechanism of electron donation by a sacrificial donor.

1.9 Fossil Fuels

Fossil fuels such as petroleum, coal, and natural gas are the primary source of energy in the world. Each one of these fuel sources has been shown to have harsh detrimental impacts on the environment as well as on the health and well-being of the human population [47,48]. Exposure to these pollutants can come from inhalation, contact, and even through ingesting contaminated food products. Many studies have shown that byproducts from the manufacture and use of fossil fuels have lead to cancers, birth defects, and even death [48]. There are also great economic impacts as well since many people are employed by the companies that provide or use these products. The burning of these products produces large amounts of dangerous byproducts that are released into the air, waterways, and soil but less commonly thought of aspects of these energy sources are the dangers and effects of producing these products.

All fossil fuels emit CO_2 as a product of combustion. Natural gas provides 24% of the energy used domestically and in doing so releases around 132 million tons of CO_2 each year [49] not taking into account the amount released during processing and transportation. Methane emissions should also be taken into account when talking about pollutants. In 1997, 75 million tons of CO_2 equivalents of methane were released as well as 118.4 tons of CO_2 transporting the coal [49].

The pollutants from fossil fuels not only come from using them but also from making or retrieving them. One has to keep in mind that it takes energy and resources to retrieve these fuels by mining or drilling. A major source of pollutants comes from the

petroleum distilleries/refineries and the processes that are required to make the crude oil useable. The distillation processes release volatile organic compounds into the surrounding environment via gaseous or liquid leaks or spills. It has been shown that certain refineries release harmful aromatic organic chemicals such as benzene, toluene and xylene into the surrounding environment in considerable quantities [47]. These chemicals are toxic and carcinogenic. Heavy metals can also be released during the various refining or consumption processes. Power plants that consume coal have been shown to release heavy metals such as mercury and other compounds as well as the other pollutants mentioned above in considerable amounts [50]. Environmental laws, as well as improving methods of preventing contamination, are slowly alleviating the issue but there are still many improvements to be made.

The rate at which the world consumes these products has been steadily increasing with the increasing world population and more energy demands and will continue to do so. Based upon the fuel reserves available, projections indicate that the reserves for coal, gas, and oil will be depleted by the years 2112, 2042, and 2040 respectively [51]. This causes a great concern and a need to develop new alternative sources of energy. While "renewable" methods for generating electric power such as solar panels, wind, and hydrothermal technologies are quickly improving they will not be able to meet the demands of the human population alone.

Much research and development has gone into the areas of bio-fuels and energy from biomass and significant advancements have been made. Biomass is anything that is organic or from biological processes such as plants and manure.

The allure of ethanol made from corn or other crops has grown stronger over recent years as the threat of diminishing fossil fuels increases. The use of widely grown crops such as corn and soy beans to produce the ethanol earns the title of "renewable resource" since it is derived from biomass [52]. It is also thought that the production and utilization of ethanol would reduce green house gasses (GHG). Several studies have been conducted and found that to be true. However, those studies did not account for the entire life cycle of the ethanol [53]. It has been determined that the production and use of bio-ethanol is worse for the environment than other forms of fuel in several areas such as air and water pollution [53,54]. The use of such crops raises concern for the agricultural community as well as the world's food supply. The availability of food has been decreasing in the world and 56% of the global population is malnourished as reported in 2008 [55]. The demand for the crops has also lead to economic concerns since the price of the crops affects many other agricultural areas, including meats and milk [53]. The benefits of using ethanol from biomass as a fuel have been misconstrued and do not outweigh the environmental and economic costs.

1.10 Hydrogen as a Fuel

As previously mentioned the supply of fossil fuels is quickly being depleted and the effects of pollution on the environment due to their use are becoming more and more apparent. The combustion of pure hydrogen with oxygen will only lead to water and energy as products. This makes the use of hydrogen as a fuel very appealing as it produces no GHGs or other pollutants. It is projected that in the near future hydrogen produced from electrolysis and photochemical reactions will be the primary long term source of hydrogen for fuel [56]. There are several different processes which aim to

produce hydrogen for a fuel source but there are many hurdles left in their paths which hinder the economical and practical applications of such methods. Studies involving the use of bacteria and plant life to biologically produce hydrogen have been conducted but have produced low rates and have not advanced significantly since the 1940s [57]. Another method that is being studied is the use of electrochemical cells and catalytic fuel cells. These cells use electricity and catalysts to produce hydrogen from water or organic substances and have the ability to reverse the process and produce electricity [58]. There are many improvements necessary to utilize hydrogen as an efficient fuel source however the largest impediment is the ability to produce hydrogen at a rate which is both efficient and economical.

1.11 Research objective

The objective of this research is to investigate (1) how the deposition of silver metal nanoparticles affects the photocatalytic activity of strontium titanate to decompose water and glycerol into hydrogen gas under different regions of the UV-Vis spectrum and (2) the mechanism by which this photocatalysis proceeds. The first objective is to determine the optimal silver loading concentration for the enhancement of photocatalytic activity of the decomposition of water and glycerol. This is done by using various optical filters and measuring the rates of hydrogen production. The second objective is to determine the electronic mechanism by which the supported metal nanoparticles aids or hinders the photocatalyst's ability to perform using spectroscopic methods and kinetic studies.

2 Experimental

2.1 Solids, Solvents, and Gases

Strontium titanate nanopowder was purchased from US Research Nanomaterials Inc. Silver nitrate was purchased from Sigma-Aldrich and Salt Lake Metals. Barium sulfate was purchased from Alfa Aesar Puratronic. The solvents used in this research are glycerol purchased from Sigma-Aldrich and distilled water provided by Rutgers University. The gases used in this research were oxygen and UHP Argon both purchased from Airgas. Calibration standards for the hydrogen having concentrations of 10, 100, and 1000 ppm in argon were also purchased from Airgas. The flow rates of the gases were controlled by mass flow controllers purchased from Omega, the argon controller had a range of 0-50 cc/min and the oxygen controller had a range of 0-10 cc/min.

2.2 Sample Preparation

In order to use the products from the reaction, the reaction mixtures were centrifuged then washed with water repeated 10 times to remove any excess silver nitrate and glycerol. Once washed the samples were dried in vacuum in the dark. In order to make the samples useable for the ex-situ spectroscopic studies, they were ground with an agate mortar and pestle by hand until a uniform consistency was achieved.

2.3 Methods of Specrtoscopic Characterization

2.3.1 Photoluminescence Spectroscopy (PL)

Photoluminescence spectroscopy was conducted using a Fluorolog spectrometer from Horiba. There were several sample holders used. For cuvettes, a temperature controlled cuvette holder provided by Horiba was used. A custom sample holder was made in order to hold quartz capillaries for the measurements of samples with limited amounts. For both pure nanocrystaline $SrTiO_3$ and the $Ag/SrTiO_3$ several photoluminescence spectra were taken. The slit widths and excitation wavelengths were varied based upon intensity and experiment.

Synchronous photoluminescence where the excitation and emission wavelengths are swept simultaneously at fixed intervals was performed in order to better resolve the fluorescent peaks of the materials. In order to determine the optimal excitation wavelengths which would produce the most define and highest intensity emission spectra, the 3-dimensional photoluminescence experiment was performed in which the spectrometer would perform a full emission spectrum scan while changing the excitation wavelengths at set intervals between each scan.

For data sets containing multiple peaks, the peaks were fit using the peak fit tool in the OriginPro 2015 data analysis program. The areas of the peak were also analyzed by the auto-integrate function.

2.3.2 Near UV-Vis Diffuse Reflectance Spectroscopy (near UV-Vis DRS)

Diffuse Reflectance spectra were measured using the Cary 5000 UV-Vis-NIR spectrometer from Agilent Technologies. In order to measure the Diffuse Reflectance spectra the Praying Mantis attachment purchased from Harrick Scientific Products Inc. was used since the powders were too optically dense to use transmission spectroscopy. The standard used for 100% reflectance was barium sulfate purchased from Alfa Aesar. The ground products were deposited in the "volcano" sample holder and the surface was packed down and leveled using a stainless steel spatula.

The spectra are reported in %Reflectance and not recalculated into the Kubelka-Munk [59] function. The Kubelka-Munk function depends on many parameters that must be kept constant. These include sample depth, scattering coefficient, particle size and density, and specular reflection [59]. However, it was necessary to use the Kubelka-Munk function in order to perform certain calculations. The spectra were measured from 200 nm to 800 nm using with an averaging time of 0.2 seconds and a data interval of 0.5 nm with a zero/baseline correction.

2.3.3 Raman Spectroscopy

Raman spectra were measured at room temperature using the Explora Plus confocal Raman microscope purchased from Horiba Scientific. The dried and ground samples were placed on the glass slides and measured using the lasers with wavelengths of 532 nm and 638 nm with varying intensities.

2.4 Characterization of nanocrystaline pure $SrTiO_3$

2.4.1 Raman Spectroscopy

In order to confirm that the $SrTiO_3$ was nanocrystaline and cubic the Raman spectrum was taken. The 638 nm laser was used for this experiment since it gave the most resolved spectrum. The accumulation was set to 100 and the 1600 grating was used.

2.4.2 Diffuse Reflectance Spectroscopy

The diffuse reflectance spectrum of pure nanocrystaline $SrTiO_3$ was taken in the Praying Mantis attachment using the "volcano" sample holder using barium sulfate as a white standard. The reflectance spectrum was taken from 200 nm to 800 nm at an interval of 0.2 nm and an integration time of 0.1 seconds in double beam mode with a reduced slit height. A zero/baseline method was used to create a more accurate baseline. The data was plotted in OriginPro 2015 and the peaks were assigned from the minima of the reflectance spectrum since the minima in the reflectance spectrum correspond to the maxima in the absorption spectrum.

2.4.3 Photoluminescence Spectroscopy

The photoluminescence spectra for the pure strontium titanate were taken in several different manners depending on the information sought. In order to screen for the optimal parameters the photoluminescence spectra were collected using three dimensional scanning. This would scan at a selected excitation wavelength then scan again with another excitation wavelength a set interval away for a range of wavelengths.

The 3D spectra for pure $SrTiO_3$ were taken in a 0.5 cc quartz cuvette with the excitation wavelength starting a 240 nm and rising to 400 nm at 10 nm increments with both of the excitation and emission slits at 2 nm and the emission being collected at 0.2 nm intervals at an integration of 0.1 seconds. For that scan the emission was collected from 250 nm to 700 nm. The empty cuvette was also scanned using the same parameters to check for any emission from the cuvette itself. As expected the cuvette showed no fluorescence in the range of interest.

Selected spectra were taken using the quartz capillary tubes so that they could be compared to the spectra of the post photocatalytic tested samples. In order to be compared to the post photocatalytic tested samples a neutral density filter was required. The transmission spectrum of the neutral density filter is shown in Figure 7.

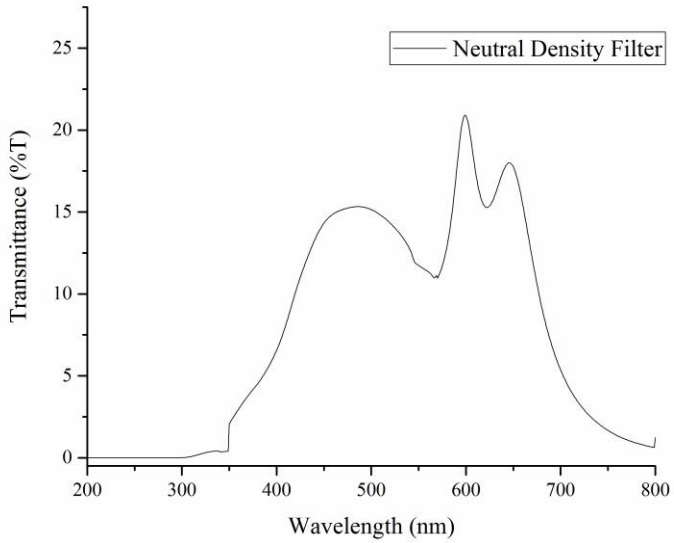

Figure 7: Transmission spectrum of the neutral density filter.

2.5 Photocatalytic Measurements

2.5.1 Photocatalytic Apparatus

Around 55.7 mg of the strontium titanate was massed and added into a quartz test tube. Then 1.5 ml of glycerol was added along with various volumes of silver nitrate stock solutions with varying concentrations then brought up to 15 ml total with distilled water and a magnetic stir bar was added into the mixture. From then until the mixture was first illuminated the mixture was kept in the dark to prevent any premature exposure to ambient light as it could begin the photocatalytic reduction of the silver. The mixture was then sonicated using a sonic cleaner for 20 minutes to help remove dissolved or adsorbed air. After sonication the reaction vessel was closed with a rubber stopper, which had two holes, one with a Teflon pipe that reached below the mixture's surface, which was used for the entrance and purge of the liquid phase with argon, and the other was near the top of the reaction vessel which was used for the outgoing gas to the sensors. The schematics for the reaction vessel are shown in Figure 8. The mixture was vacuum degassed for 20 minutes to further remove dissolved gas, then back filled with argon to prevent any unwanted air from entering. The mixture was stirred with a constant rate during all of the reactions.

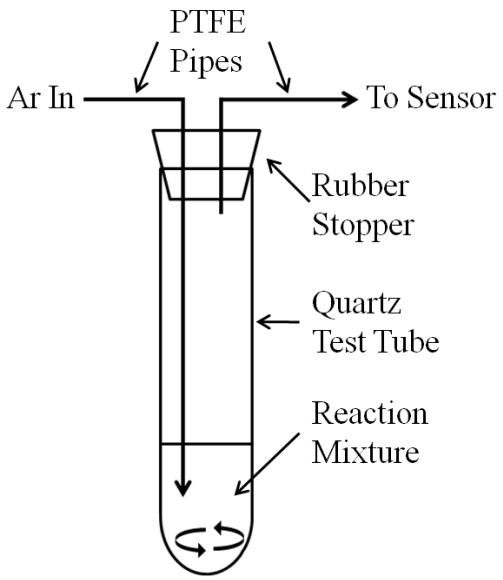

Figure 8: Schematics for the photocatalytic reaction vessel.

The photocatalytic tests were performed using a 450 W medium pressure mercury vapor lamp and a custom apparatus. To prevent any artifacts from back-scattered light a custom housing was built which covered the entire reaction vessel except for a 4 cm by 4 cm window. This housing was necessary in order to prevent any unwanted light from hitting the reaction vessel that was not filtered when using the filters and also to keep the amount of light hitting the reaction vessel constant.

2.5.2 Measurement of Hydrogen Concentration

For the measurement of the amounts and concentration of the hydrogen produced in our experiments a 4-20 mAmp hydrogen sensor from Sierra Monitor Corporation model 4101-07 was used [60]. A periodic sampling method was used in which the reaction mixture was illuminated for different amounts of time while the reaction vessel was sealed. Once the illumination time was reached the light was blocked from hitting

the reaction vessel as to prevent any additional hydrogen from being produced while measuring the amount of hydrogen produced during the earlier illumination time. The reaction mixture was then purged with argon at 40 cc/min and sent to the sensor until the signal returned to the baseline. In order to provide adequate oxygen to the sensor, while the sensor from Sierra Monitor model 4101-7 was used, oxygen was pre-mixed with the sample downstream of the reactor at 10 cc/min. After the signal returned to the base line, the reactor was then closed again and the light shield was removed. This process was repeated several times to monitor the rate at which hydrogen was being produced [61]. Figure 9 shows a typical output signal using this method and sensor. This produced several peaks which were then integrated using the OriginPro 2015 software and recalculated from Volt*seconds into μmol/(hour*gram) using a calibration curve and the mass of the catalyst used (see Appendix for calculation section details). The calibration curve used for these calculations is shown in the Appendix Figure 1.

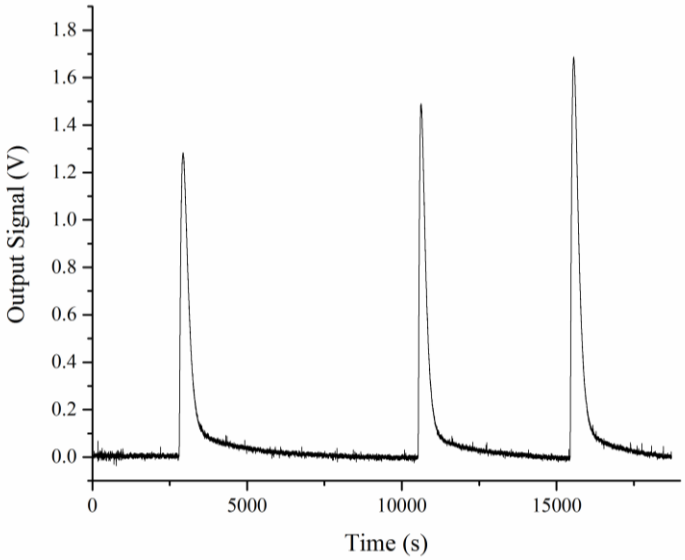

Figure 9: Typical signal output from Sierra Monitor model 4101-7 sensor.

2.5.3 Hydrogen Production and In-situ Silver Deposition

Several concentrations of silver nitrate were used to determine the effect of different metal loadings on the metal which correspond to molar ratios of 0, 0.1:100, 1:100, 5:100, 10:100, 15:100, 20:100, and 50:100 mol Ag:mol $SrTiO_3$. Each of these samples was subjected to illumination under optically unfiltered, λ>375 nm, and λ>400 nm illumination from the mercury lamp in order to measure the activity of the photocatalysts in the corresponding regions of light. The filters used were a 375 nm cutoff filter 7380 from Ace Glass and a 400 nm cutoff filter also from Ace Glass. The spectral distribution of the lamp with the different filters is shown in Figure 10 (explanation of spectra is in the Appendix).

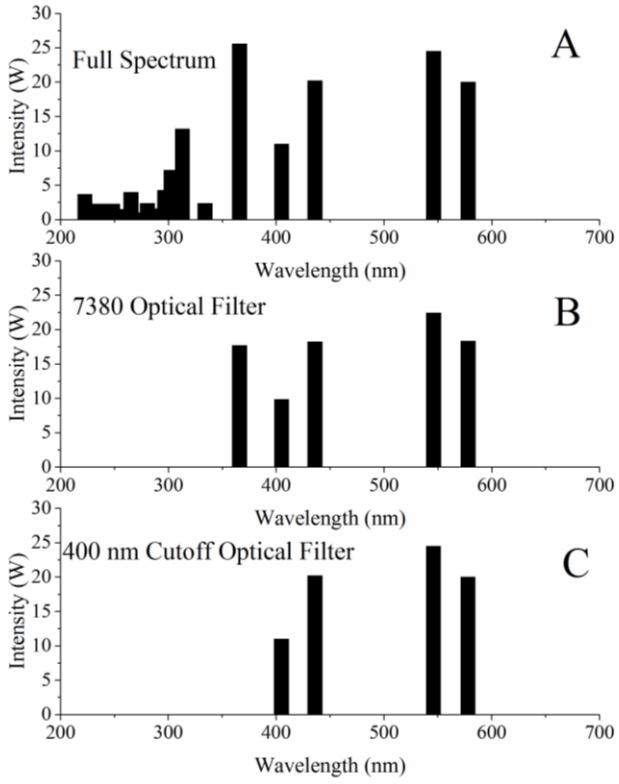

Figure 10: Spectral distributions of the mercury lamp under the different optical filters.

2.6 Post Catalysis Characterization

2.6.1 Sample Preparation

In order to perform ex-situ characterization techniques on the silver deposited Ag:$SrTiO_3$ after the catalytic testing the reaction mixtures had to be centrifuged and washed with distilled water 10 times to remove any excess glycerol or silver nitrate present. This was done with the minimal amount of light and air exposure as to prevent the products from being chemically altered by oxidation or further light exposure. Once the washing was complete the products were dried and stored in a vacuum chamber to also reduce the exposure to air. The dried powders had to be ground using an agate mortar and pestle until a uniform consistency was achieved so that they could be used in the spectrometers.

2.6.2 Diffuse Reflectance Spectroscopy

The diffuse reflectance spectra were taken using the Praying Mantis accessory with the "volcano" sample holder. Barium sulfate was used as a white 100 % reflectance standard. The Ag:$SrTiO_3$ sample used in this analysis was the 10:100 Ag:$SrTiO_3$ silver photocatalysts. The reflectance spectra were collected from 200 nm to 800 nm at an interval of 0.2 nm and an integration time of 0.1 seconds in double beam mode with a reduced slit height. A zero/baseline method was used to create a more accurate baseline. These were the same parameters used for the spectra obtained for nanocrystaline $SrTiO_3$ so that the spectra could be compared to each other.

2.6.3 Photoluminescence Spectroscopy

Since there were small amounts of the photocatalysts that were able to be recovered after the photocatalytic testing the photo luminescence spectra had to be taken in the quartz capillary. These spectra were taken for the 10:100 Ag:$SrTiO_3$. 3D photoluminescence spectra were taken with the excitation wavelengths starting at 300 nm and ending at 400 nm with 5 nm steps. Both the excitation and emission slits were set at 3 nm and the emission was collected from 310 nm to 700 nm at 0.5 nm increments. The integration time was 0.1 seconds.

3 Results

3.1 Characterization of Pure $SrTiO_3$

3.1.1 Raman Spectroscopy

Cubic strontium titanate has a space group of Pm3m, which would correspond to a symmetry of $3F_{1u} + F_{2u}$ and neither of these symmetries are first order Raman-active modes due to the center of symmetry causing zero polarizability of the lattice [62,63]. Since a Raman spectrum from strontium titanate can be obtained, there have been many recent reports that study this phenomenon. It has been determined that the vibrational modes are modified by several factors such as oxygen vacancies, long range electrostatic factors, and other external factors [63]. This causes the appearance of new vibrational modes which, in the case of cubic strontium titanate, the F_{2u} splits into a nondegenerate A_1 mode and the F_{1u} modes split into a doubly degenerate E mode and a nondegenerate A_1 mode [63]. Long range electrostatic forces can also further separate the different modes [64]. In the case of strontium titanate these forces separate the E and A_1 modes into longitudinal optical (LO) and transverse optical (TO) modes [62]. This splitting and mixing of vibrational modes causes the Raman spectrum of strontium titanate to have broad peaks.

As previously mentioned the Raman spectrum of pure $SrTiO_3$ was taken using an 638 nm excitation laser at room temperature from a Raman shift of 200 cm^{-1} to 1150 cm^{-1}. Figure 11 shows the obtained Raman spectrum of strontium titanate. It can be seen that the different vibrational modes previously mentioned that are within the measured range appear in the spectrum. The assignments for the observed peaks are listed in Table

4. The peak at 1074 cm^{-1} is due to strontium carbonate impurities which has been previously reported [63]. The 800 cm^{-1} and 270 cm^{-1} peaks appear as shoulders.

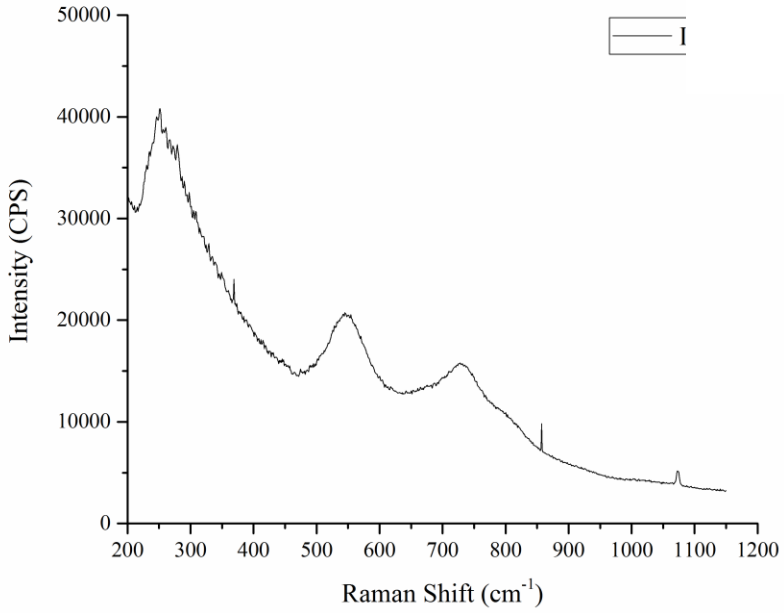

Figure 11: Raman spectrum of pure strontium titanate collected at room temperature using 638 nm as the excitation laser.

Table 4: Assignments of the Raman peaks for strontium titanate measured using an excitation wavelength of 638 nm and their vibrational mode assignments [63].

Obtained values (cm^{-1})	Reported values (cm^{-1})	Vibrational mode
270	270	TO_3
544	544	TO_4
727	727	TO
800	801	LO_4
1074	1074	$SrCO_3$

3.1.2 Diffuse Reflectance Spectroscopy

The diffuse reflectance spectrum was obtained for the purchased nanocrystaline $SrTiO_3$ from 200 nm to 800 nm using barium sulfate as a reference. Figure 12 shows the obtained reflectance spectrum. The reflectance spectrum shows a strong absorption between 200 nm and 350 nm with small "humps" at around 250 nm and 300 nm then nearly no absorption from 400 nm and above which agrees with reported spectra [6,19]. The lack of absorption in the visible region is expected since the powder is optically white. This also explains the lack of activity in the visible range since there is no absorption in that region. The agreement between our obtained spectrum and the reported spectra confirm that the spectroscopic method used was acceptable

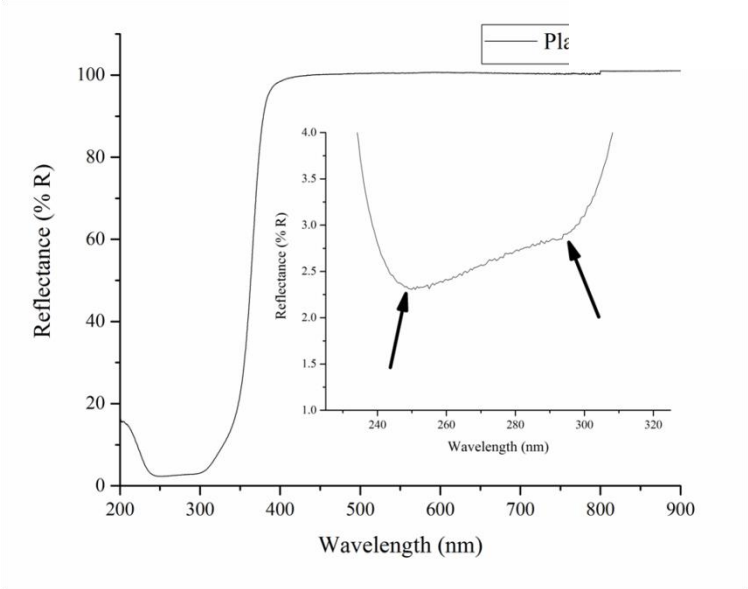

Figure 12: DRS spectrum for pure $SrTiO_3$. Inset showing two "humps" at 250 nm and 300 nm

Using the obtained spectrum the reflectance was recalculated into Tauc plots as to further investigate the energy levels present within the pure strontium titanate. Tauc plots

are frequently used to determine the optical band gap of different materials [65]. This is done by using the formula $(\alpha*E)^{1/n} = E - E_g$, where α is an absorption coefficient, n is the Tauc constant, E is the photon energy and E_g is an optical band gap [66]. For powdered semiconductors the Tauc plots can constructed from the reflectance by first applying the Kubelka-Munk function [66]. In order to find the direct optical band gap the coefficient becomes n= ½ and for the indirect band gap it becomes n=2 [65]. It was found that there is a direct band gap at 3.87 eV and an indirect band gap at 3.30 eV which correspond to 320 nm and 375 nm respectively as shown in Figure 13.

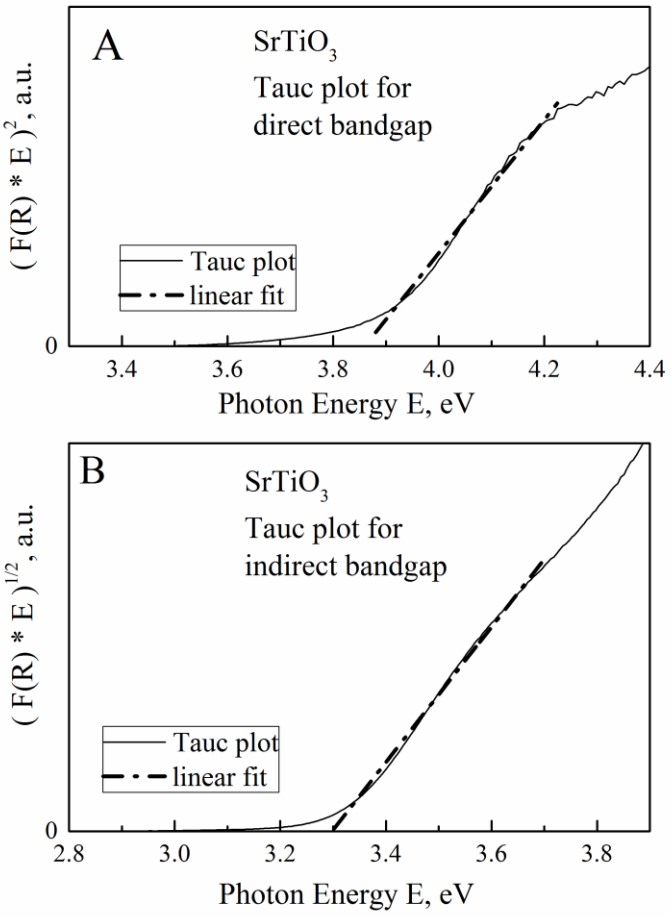

Figure 13: Tauc plot for the (A) direct band gap and (B) indirect band gap of pure $SrTiO_3$

3.1.3 Photoluminescence Spectroscopy

The photoluminescence spectra for pure $SrTiO_3$ were collected in several manners. 3D photoluminescence was used to determine the optimal excitation wavelengths which would give the most intense emission spectra so that the powders could be better characterized. The change in excitation wavelength also would affect the amount and positions of the emission peaks which allowed for better resolution of the energy transitions. The spectra were taken using quartz capillary tubes and a neutral density filter. Figure 14 shows the photoluminescence spectrum of pure $SrTiO_3$ with an excitation wavelength of 380 nm, which has an energy of 3.26 eV, which would excite the indirect band gap. The maxima of the above spectra that were determined by mathematical fitting are 450 nm and a shoulder at 500 nm which correspond to 2.76 eV and 2.48 eV respectively. These peaks are due to the presence of oxygen vacancies within the lattice structure as previously confirmed in literature [67,68]. These oxygen vacancies create energy levels below the conduction band. There are also energy states above the valence band which allow the electrons to be excited by photons of lower energy than the band gap. This explains the photoluminescence obtained when using lower energy excitation wavelengths.

When using 420 nm, corresponding to an energy of 2.95 eV which is well below the band gap of $SrTiO_3$, as the excitation wavelength the spectrum shows a maximum at 500 nm, corresponding to an energy of 2.48 eV, as shown in Figure 15. The ability to photoluminescence using an excitation wavelength with an energy below the band gap is due to the excitation of an electron in the valence band of $SrTiO_3$ into defect states below

the conduction band [68]. These delocalized orbitals are the result of broken bonds intrinsic in nano-powders and act as optical absorption centers [69].

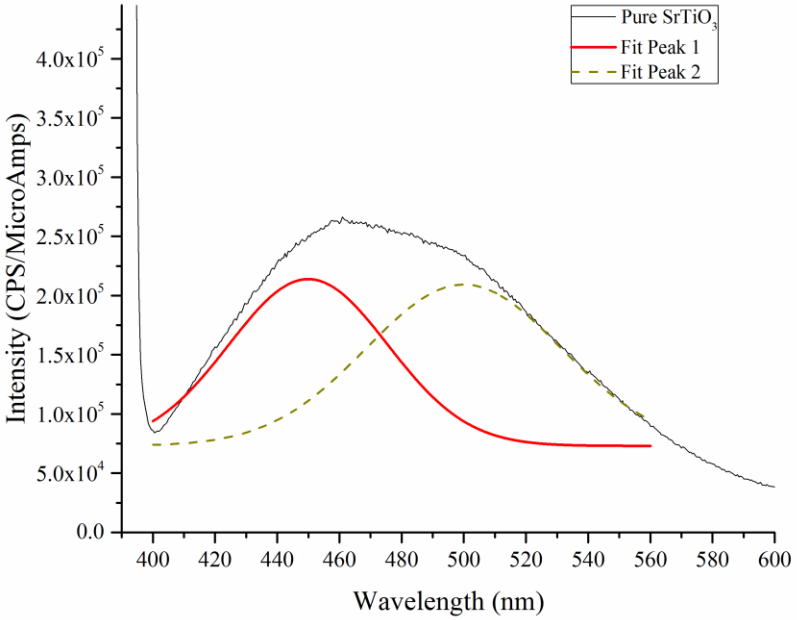

Figure 14: Photoluminescence spectrum of pure $SrTiO_3$ using 380 nm as the excitation wavelength and the neutral density filter.

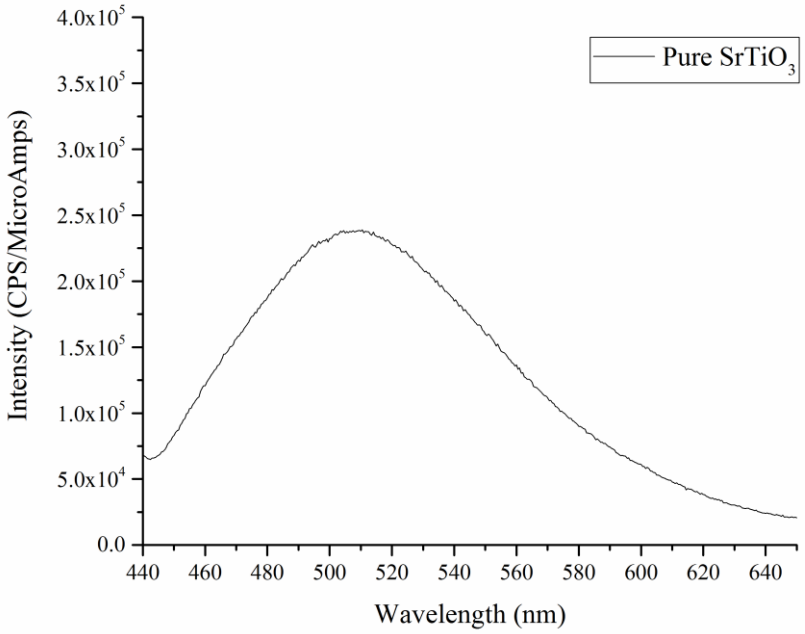

Figure 15: Photoluminescence spectrum of pure $SrTiO_3$ using 420 nm as the excitation wavelength and the neutral density filter.

Figure 16 shows the mechanism by which the photoluminescence is occurring. The "blue" emission seen using the 380 nm excitation wavelength is due to the excited electron relaxing from the conduction band of the strontium titanate to the oxygen energy states above the valence band of the strontium titanate then nonradiatively relaxing to the valence band. The "green" emission is due to the electron relaxing nonradiatively to the oxygen defect energy levels below the conduction band then further relaxing to the oxygen states above the valence band then again relaxing nonradiatively to the valence band. When using the excitation wavelength of 420 nm the "blue" emission is no longer seen since the excitation energy is too low for the electron to reach the conduction band

but instead moves to the oxygen vacancy states below the conduction band and relaxing to the lower oxygen states then again relaxes to the valence band nonradiatively.

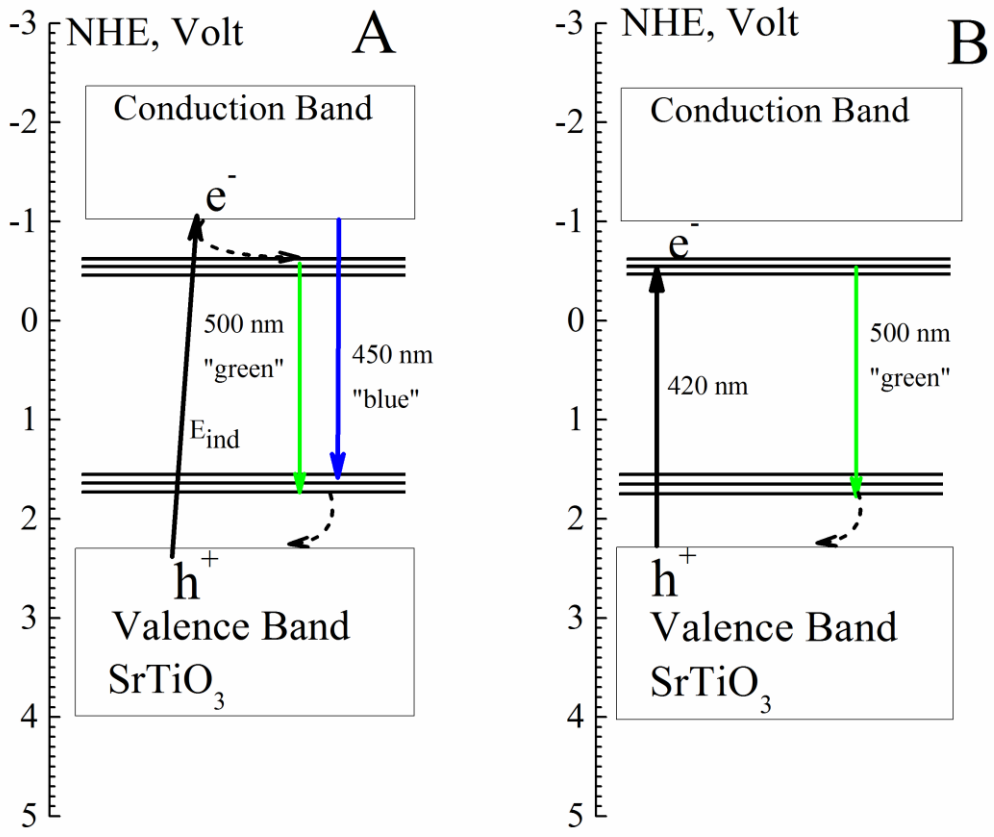

Figure 16: Diagram of the energy transitions determined from the photoluminescence spectra of strontium titanate using the excitation wavelengths of A) 380 nm and B) 420 nm

3.2 Photocatalytic Hydrogen Generation

The photocatalytic testing was performed by the above method detailed in the experimental section. The rates for the optically filtered light exposures were measured using the Seirra Monitor sensor by using the periodic sampling method. The reaction mixture was illuminated using the different optical filters for a set amount of time then the light was blocked and the reaction vessel was purged to the sensor allowing for the

measurement of the amount of hydrogen produced during that time. The method by which the signal obtained from the sensor was converted is detailed in the supplementary section.

3.2.1 Photocatalytic Activity with Optically Unfiltered Light

For the unfiltered light exposure several peaks were obtained in order to confirm the maximum production was reached and no further increase in activity would go unnoticed. For unfiltered light the silver loadings that were tested were 0, 1:100, 5:100, 10:100, 15:100, 20:100, and 50:100 molar ratios of Ag:$SrTiO_3$. Figure 17 shows a graph of hydrogen production rate versus silver loading and Table 5 shows the numerical values of the hydrogen production rates for each concentration of silver loading. It is shown that the photocatalytic rate has a bimodal dependence on the amount of silver loading. This type of dependence has been previously reported for another photocatalyst [28] however no analysis was published. It is suggested that the reason for the decreases of activity at higher Ag loadings is due to the optical absorption of the silver nanoparticles being too large which prevents the light from reaching the semiconductor photocatalyst hindering catalytic activity. The optimal loading of silver as seen in the graph was 1:100 Ag:$SrTiO_3$ molar ratio. The error bars cannot be seen on the graph due to the scale of the graph.

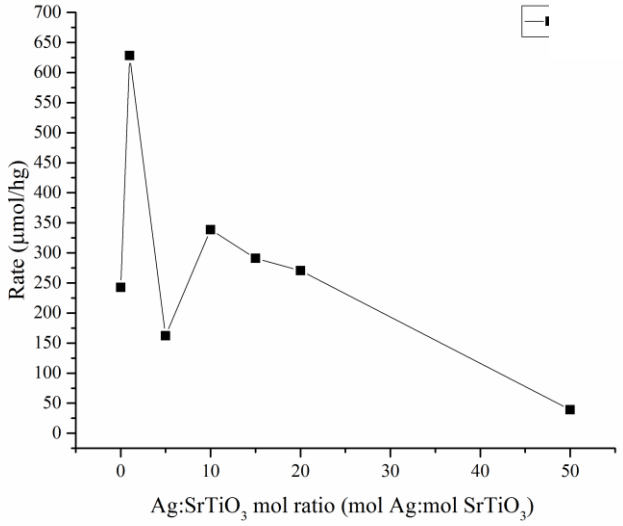

Figure 17: Graph of the rate of photocatalytic hydrogen production versus the $Ag:SrTiO_3$ mol ratio for unfiltered illumination

Table 5: Numerical photocatalytic hydrogen production rates of $Ag:SrTiO_3$ mol ratio for optically unfiltered light

mol Ag per 100mol $SrTiO_3$	Hydrogen production Rate $\mu mol*h^{-1}*g^{-1}$	Error $\mu mol*h^{-1}*g^{-1}$
0	242.5	±6.8
1	628.3	±9.5
5	162.2	±6.5
10	338.7	±8.3
15	291.0	±5.6
20	270.5	±7.4
50	39.2	±2.6

3.2.2 Photocatalytic Activity with Near UV and Visible Light (Optical filter #7380, λ>375 nm)

The rates of hydrogen production for the 375 nm cutoff filter were obtained in the same method as in the unfiltered light except with the 7380 filter from Ace Glass filtering the light entering the reaction vessel. During these experiments the $SrTiO_3$ indirect band gap was still excited since there were still some wavelengths in the UV range that were reaching the reaction vessel. Figure 18 and Table 6 show the graphical representation and the numerical values of the photocatalytic rates of the various silver loadings respectively. The metal loadings used for this filtered light were the same as the loadings used for the unfiltered light with the addition of 0.1:100 Ag:$SrTiO_3$ molar ratio. It can be seen that the same bimodal phenomenon occurred for the 375 nm cutoff filtered photocatalysis as in the unfiltered photocatalytic tests. There is a sharp decrease down to zero between 15:100 and 20:100 Ag:$SrTiO_3$ molar ratios which indicates that there was a severe over loading effect preventing the light from reaching the $SrTiO_3$. Again the lower silver loadings were more efficient than the higher loadings.

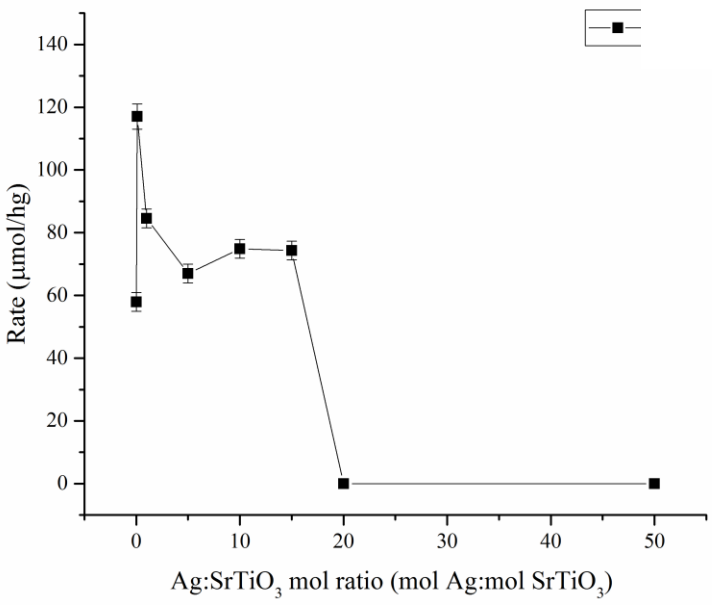

Figure 18: Graph of the rate of photocatalytic hydrogen production versus the $Ag:SrTiO_3$ mol ratio for near UV and Visible light (optical filter 7380 λ>375 nm)

Table 6: Numerical photocatalytic hydrogen production rates of Ag:$SrTiO_3$ mol ratio for near UV and Visible light (optical filter 7380, λ>375 nm)

mol Ag per 100mol $SrTiO_3$	Hydrogen production Rate $\mu mol*h^{-1}*g^{-1}$	Error $\mu mol*h^{-1}*g^{-1}$
0	57.9	±2.8
0.1	117.0	±3.5
1	84.5	±3.1
5	67.0	±2.8
10	74.8	±3.1
15	74.3	±2.7
20	0	±0
50	0	±0

3.2.3 Photocatalytic Activity with Visible Light (λ>400 nm Filter)

The photocatalytic tests for the 400 nm cutoff filter were performed in the same manner as those for the 375 nm cutoff filter. The graphical representation of the photocatalytic rates and a table of their numerical values are shown in Figure 19 and Table 7 respectively. Just as in the other two data sets the lower silver loadings give higher rates than the higher loadings because of the same reason as mentioned before. As expected the hydrogen production rates for the visible light are significantly lower than those for the full spectrum and the 375 nm cutoff filter since the $SrTiO_3$ is no longer being excited directly by the light. The main difference with this section of tests is that the 5:100 Ag:$SrTiO_3$ molar ratio is the highest which contrasts the previous data. Our

working hypothesis for this phenomenon is that since the semiconductor is no longer being excited the hydrogen production rate depends largely on the plasmonic properties of the deposited silver nanoparticles. As previously stated the plasmonic properties depend on the size of the nanoparticles which is affected by the amount of silver ions present in the solution available to be reduced. When the loading is too high both the light shielding effect and the size of the nanoparticles affect the ability for photocatalysis to be performed. The fact that the 5:100 Ag:$SrTiO_3$ molar ratio was the highest in activity could be due to the increased amount of nanoparticles on the surface of the $SrTiO_3$ then once any more silver is added the surface becomes over crowded the plasmonic properties are hindered.

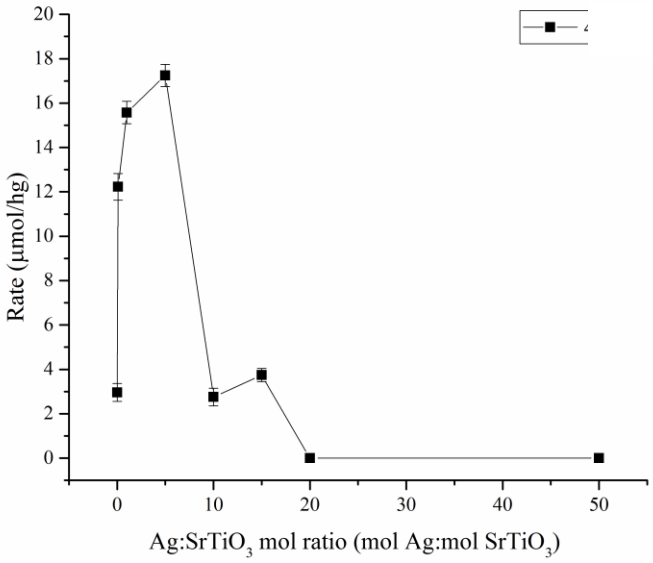

Figure 19: Graph of the rate of photocatalytic hydrogen production versus the Ag:$SrTiO_3$ mol ratio for Visible light (λ>400 nm)

Table 7: Numerical photocatalytic hydrogen production rates of Ag:$SrTiO_3$ mol ratio for Visible light (λ>400 nm)

mol Ag per 100mol $SrTiO_3$	Hydrogen production Rate $\mu mol*h^{-1}*g^{-1}$	Error $\mu mol*h^{-1}*g^{-1}$
0	3.0	±0.4
0.1	12.2	±0.6
1	15.6	±0.5
5	17.2	±0.5
10	2.8	±0.4
15	3.7	±0.3
20	0	±0
50	0	±0

4 Post-Photocatalytic Characterization

4.1 Diffuse Reflectance Spectroscopy

The diffuse reflectance spectrum for 10:100 Ag:$SrTiO_3$ molar ratio was taken after it was photocatalytically tested, washed, and dried as detailed above. This was done in order to determine that the silver plasmonic peak was present in the sample. The middle concentration of silver was used for this spectroscopic method to assure that the spectrometer would be able to resolve the plasmonic peaks and that they would not be hidden or altered by the strong absorption of the $SrTiO_3$ which is near the location of the plasmonic peak for silver nanoparticles. The reflectance spectrum was obtained using the same settings and processes as those for the nanocrystaline $SrTiO_3$ so that they could be directly compared to each other. Figure 20 shows the reflectance spectrum for 10:100 Ag:$SrTiO_3$ molar ratio. The minima from the $SrTiO_3$ remain the same as the nanocrystaline $SrTiO_3$ and appear unaltered by the presence of the silver nanoparticles. As shown in the reflectance spectrum for the 10:100 Ag:$SrTiO_3$ molar ratio there is a new broad minimum which corresponds to an absorption maximum centered at 446 nm which is 2.78 eV. This confirms the presence of plasmonic silver nanoparticles that are slightly larger than 40 nm in diameter since it agrees with previously reported values [15]. A Tauc plot was calculated for the indirect band gap and it was found that the indirect band gap was 3.20 eV as shown in Figure 21. Therefore, no band gap modification in strontium titanate has occurred after photodeposition of metallic silver nanoparticles.

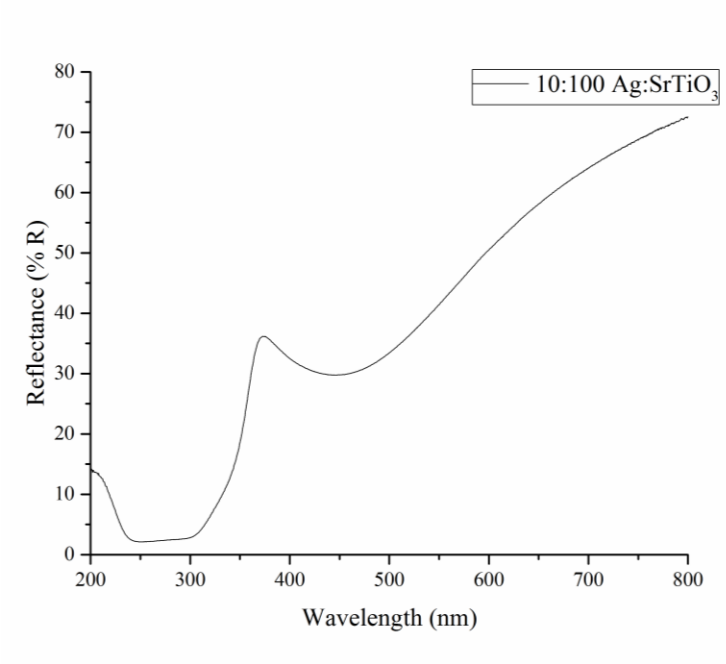

Figure 20: Diffuse Reflectance spectrum for 10:100 Ag:$SrTiO_3$

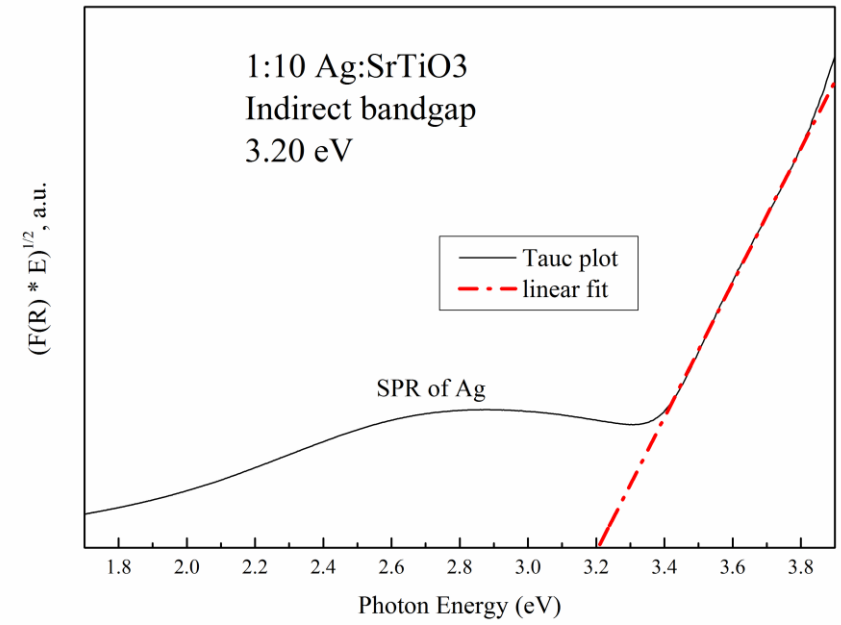

Figure 21: Tauc plot for the indirect band gap of 10:100 Ag:$SrTiO_3$

4.2 Ex-situ Photoluminescence Testing

The photoluminescence spectra for 10:100 Ag:$SrTiO_3$ were taken using the quartz capillary tube and the neutral density filter. The filter was used because the sample would begin to decompose if it was exposed to intense excitation light in the presence of air. When using 380 nm as the excitation wavelength the obtained spectrum had the same intensity of as the pure $SrTiO_3$ however it was slightly red shifted as shown in Figure 22.

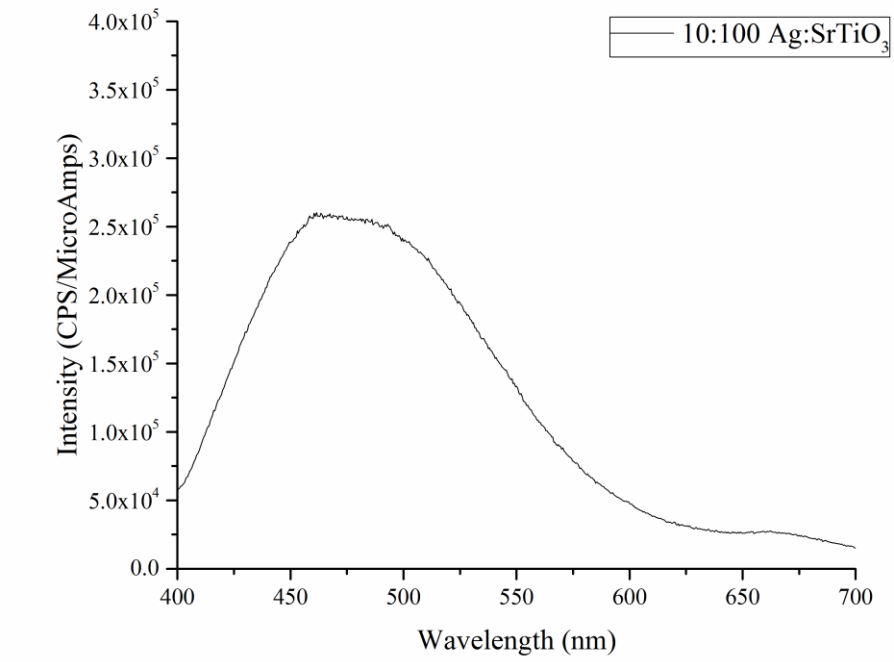

Figure 22: Photoluminescence spectrum of 10:100 Ag:$SrTiO_3$ mol ratio using the neutral density filter and 380 nm as the excitation wavelength.

Upon excitation with 420 nm the photoluminescence intensity decreased significantly as shown in Figure 23 which is a direct comparison of the 10:100 Ag:$SrTiO_3$

to the pure $SrTiO_3$. The quenching of the 500 nm peak is due to the silver nanoparticle acting as a nonradiative pathway for relaxation. When the 420 nm excitation wavelength is used, as previously stated, the electron moves into the oxygen vacancy states instead of the conduction band. From there the electron relaxes nonradiatively into the energy band of the silver nanoparticle where it then relaxes back into the valence band of strontium titanate thus bypassing the "green" emission route as shown in Figure 24.

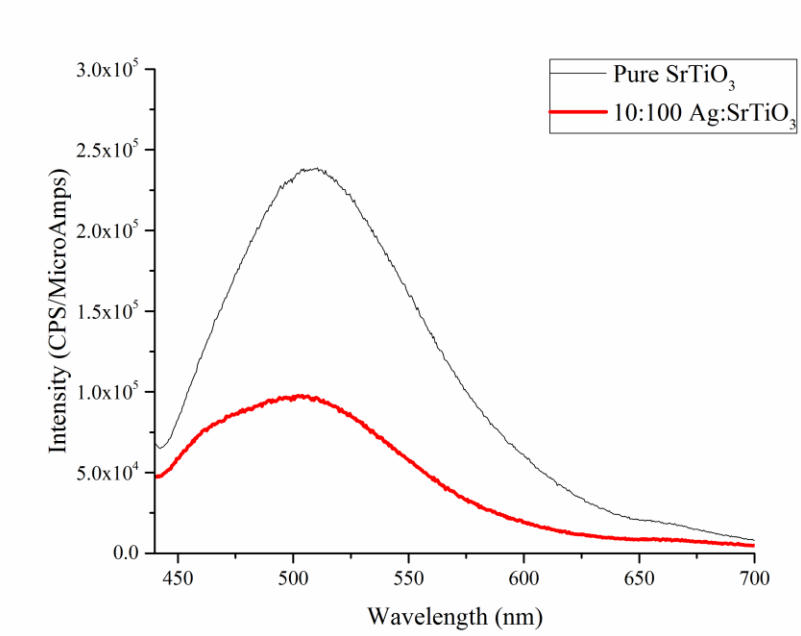

Figure 23: Comparison of the photoluminescence spectra obtained using 420 nm excitation wavelength of pure $SrTiO_3$ and 10:100 Ag:$SrTiO_3$

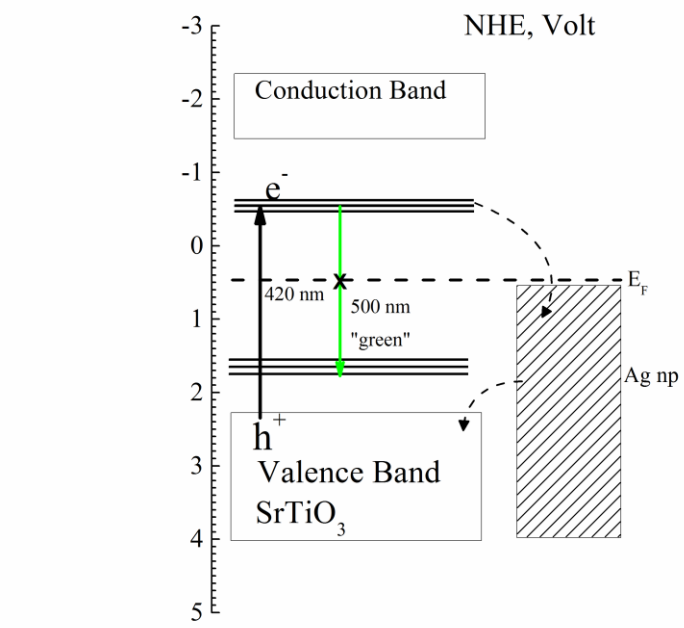

Figure 24: Diagram of the photoluminescence quenching of the 500 nm emission peak due to the silver nanoparticle upon excitation with 420 nm

4.3 In-situ Photoluminescence Spectroscopy Experiment

The rate of silver deposition was monitored using the photoluminescence spectroscopy by using the 373 nm excitation light to mimic the photocatalytic tests. A 3 ml cuvette was filled with the appropriate amounts to make a 1:10 Ag:$SrTiO_3$ molar ratio and then the remaining volume was filled with 10 vol% glycerol/water solution. While stirring the reaction mixture, the emission spectra were collected at 5 minute intervals using 373 nm as the excitation wavelength since this is close to an intense line in the emission spectrum of the mercury lamp at 366 nm. The fluorescence intensity of the 444 nm emission peak of strontium titanate was monitored as time progressed and the intensity of said peak versus time is shown in Figure 25. The peak from strontium titanate was quickly quenched within the first 10 minutes then continued to decrease more slowly

over the next 30 minutes. This indicates that the deposition of silver onto the surface and electronically interacting with the strontium titanate requires an extended activation period before the final form of the photocatalyst is produced.

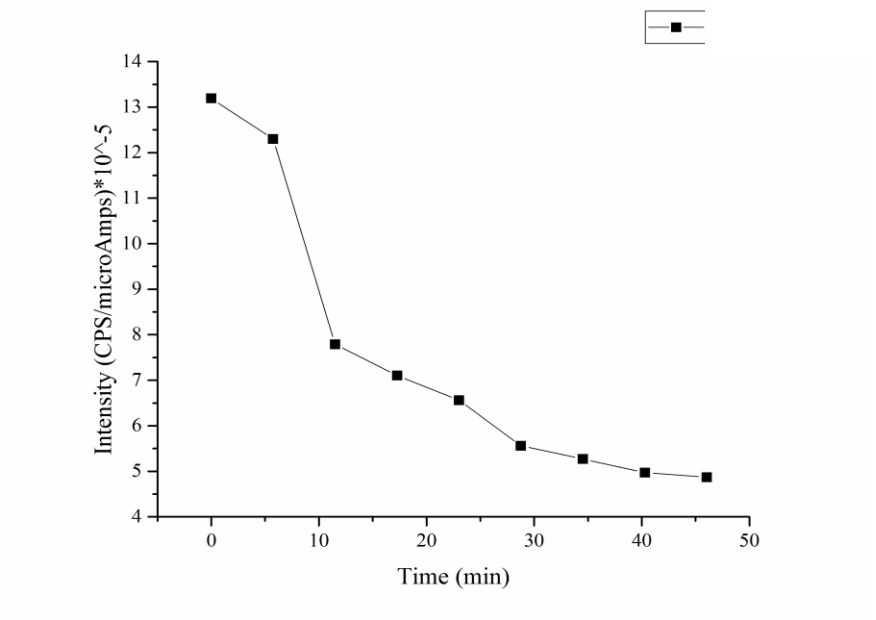

Figure 25: Graph of PL intensity of 444 nm peak against time for 10:100 Ag:$SrTiO_3$ at 5 minute intervals under constant excitation at 373 nm

5 Conclusions

We have studied the effect that photocatalytically depositing plasmonic silver metal nanoparticles onto the surface of $SrTiO_3$ has on the photocatalytic rate of hydrogen evolution from an aqueous glycerol solution. We have also studied how the amount of silver deposited on the $SrTiO_3$ surface affects the photocatalytic performance of the composite photocatalysts in the three regions of photoexcitation. The following are the major findings we have obtained.

In this research it was found that photocatalytically depositing silver metal nanoparticles on the surface of $SrTiO_3$ using an in-situ method affected the photocatalytic hydrogen production rate depending on the amount of silver loading. The rates were obtained using the three optical regions of light to study the different proposed mechanisms. It was found that the lower metal loadings increased the rate of hydrogen production and the higher loadings increased then decreased the rate of hydrogen production in all three regions of light studied. This is due to overloading the catalysts with silver nanoparticles caused an increase in absorption blocking the light from getting to the catalyst thus hindering photocatalysis. We have proposed that the smaller metal loadings promote photocatalysis by allowing for the plasmonic photoinjection of an electron from the nanoparticle into the semiconductor. We have also shown by PL quenching that the metal nanoparticles act as charge trapping sites which delay electron-hole recombination and allow for more efficient photocatalysis.

The presence of the silver nanoparticles was confirmed by UV-Vis Diffuse Reflectance Spectroscopy, and Photoluminescence spectroscopy. There was significant quenching of the emission peak from $SrTiO_3$ upon deposition of the silver nanoparticles.

6 Future Plans

In the future we would further investigate the mechanism by which the silver nanoparticles participate in photocatalysis by more advanced spectroscopic methods. We would also study how the rate of photocatalytic hydrogen production is affected by the rate of silver nanoparticle deposition. This can be done by using custom reaction chambers that would allow for the measurement of hydrogen in real time as photoluminescence spectra are taken.

We would also like to investigate the mechanism by which the glycerol aids in photocatalytic production of hydrogen. This would be done by examining the contents of the supernatant after longer photocatalytic tests. We would use NMR spectroscopy to determine if any oxidation products of glycerol were present and determine their concentrations in order to further investigate the electron donation process.

Appendix

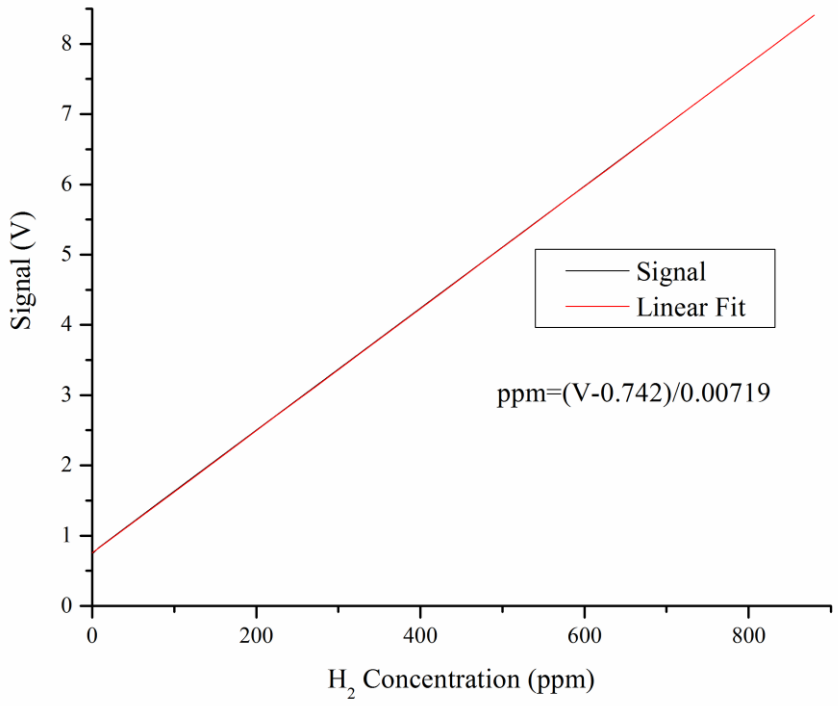

Appendix Figure 1: Calibration curve relating voltage to ppm of H_2

Explanation of Conversion from Signal to ppmH_2

In order to convert the signal from the sensor into μmol/hg several steps were taken. First the voltage signal from the sensor was converted to ppm of H_2 using the calibration curve made using 10 ppm, 100 ppm, and 1000 ppm H_2 in argon under the same conditions as the photocatalytic experiments were under. Once the signal was converted into ppm H_2 it was again recalculated into μmol/s H_2 using the flow rate of the

argon and the molar volume of a gas. Once the data was in μmol/s it was integrated so that the total number of mols of H_2 produced in that period was determined. The number of mols H_2 was then divided by the time of exposure to the mercury lamp for that run and again divided by the mass of catalyst used in that experiment which finally results in the units of μmol/hg (μmol H_2*$hour^{-1}$*$gram^{-1}$).

Explanation of Hg Lamp Spectral Distributions Under the Optical Filters

The intensities of the spectral lines from the Hg vapor lamp were obtained from the manufacturer. Then the %Transmittance spectrum for each of the optical filters was obtained. The obtained percentages were then applied to the intensities of the spectral lines of the Hg lamp to obtain the intensities of the spectral lines after passing through the optical filters.

References

[1] K. Nomura, H. Ohta, K. Ueda, T. Kamiya, M. Hirano, H. Hosono, Thin-film transistor fabricated in single-crystalline transparent oxide semiconductor, Science. 300 (2003) 1269-1272.

[2] B. Zieliñska, E. Borowiak-Palen, R.J. Kalenczuk, Photocatalytic hydrogen generation over alkaline-earth titanates in the presence of electron donors, Int J Hydrogen Energ. 33 (2008) 1797-1802.

[3] X. Chen, S. Shen, L. Guo, S.S. Mao, Semiconductor-based photocatalytic hydrogen generation, Chem Rev. 110 (2010) 6503-6570.

[4] H.W. Kang, S.B. Park, Preparation of novel $SrTiO_3$:Rh/Ta photocatalyst by spray pyrolysis and its activity for H_2 evolution from aqueous methanol solution under visible light, Int J Hydrogen Energ. 38 (2013) 823-831.

[5] J. Zou, L. Zhang, S. Luo, L. Leng, X. Luo, M. Zhang, Y. Luo, G. Guo, Preparation and photocatalytic activities of two new Zn-doped $SrTiO_3$ and $BaTiO_3$ photocatalysts for hydrogen production from water without cocatalysts loading, Int J Hydrogen Energ. 37 (2012) 17068-17077.

[6] T. Puangpetch, T. Sreethawong, S. Yoshikawa, S. Chavadej, Hydrogen production from photocatalytic water splitting over mesoporous-assembled $SrTiO_3$ nanocrystal-based photocatalysts, J Mol Catal A: Chem. 312 (2009) 97-106.

[7] T. Puangpetch, T. Sreethawong, S. Yoshikawa, S. Chavadej, Synthesis and photocatalytic activity in methyl orange degradation of mesoporous-assembled $SrTiO_3$ nanocrystals prepared by sol–gel method with the aid of structure-directing surfactant, J Mol Catal A: Chem. 287 (2008) 70-79.

[8] A. Chongterdtoonskul, J.W. Schwank, S. Chavadej, Comparative study on the influence of second metals on Ag-loaded mesoporous $SrTiO_3$ catalysts for ethylene oxide evolution, J Mol Catal A: Chem. 372 (2013) 175-182.

[9] H.W. Kang, S.B. Park, H_2 evolution under visible light irradiation from aqueous methanol solution on $SrTiO_3$:Cr/Ta prepared by spray pyrolysis from polymeric precursor, Int J Hydrogen Energ. 36 (2011) 9496-9504.

[10] H.W. Kang, S.N. Lim, D. Song, S.B. Park, Organic-inorganic composite of g-C_3N_4–$SrTiO_3$:Rh photocatalyst for improved H_2 evolution under visible light irradiation, Int J Hydrogen Energ. 37 (2012) 11602-11610.

[11] K. Maeda, Rhodium-doped barium titanate perovskite as a stable p-type semiconductor photocatalyst for hydrogen evolution under visible light, ACS Appl Mat Inter. 6 (2014) 2167-2173.

[12] T. Puangpetch, T. Sreethawong, S. Chavadej, Hydrogen production over metal-loaded mesoporous-assembled $SrTiO_3$ nanocrystal photocatalysts: effects of metal type and loading, Int J Hydrogen Energ. 35 (2010) 6531-6540.

[13] T. Puangpetch, P. Sommakettarin, S. Chavadej, T. Sreethawong, Hydrogen production from water splitting over Eosin Y-sensitized mesoporous-assembled perovskite titanate nanocrystal photocatalysts under visible light irradiation, Int J Hydrogen Energ. 35 (2010) 12428-12442.

[14] M. Ni, M.K. Leung, D.Y. Leung, K. Sumathy, A review and recent developments in photocatalytic water-splitting using TiO_2 for hydrogen production, Renew Sust Energ Rev. 11 (2007) 401-425.

[15] S. Linic, P. Christopher, D.B. Ingram, Plasmonic-metal nanostructures for efficient conversion of solar to chemical energy, Nat Mater. 10 (2011) 911-921.

[16] A.O. Govorov, H. Zhang, Y.K. Gun'ko, Theory of photoinjection of hot plasmonic carriers from metal nanostructures into semiconductors and surface molecules, J Phys Chem C. 117 (2013) 16616-16631.

[17] H. Muta, A. Ieda, K. Kurosaki, S. Yamanaka, Substitution effect on the thermoelectric properties of alkaline earth titanate, Mater Lett. 58 (2004) 3868-3871.

[18] V. Kumar, Solution-Precipitation of Fine Powders of Barium Titanate and Strontium Titanate, J Am Ceram Soc. 82 (1999) 2580-2584.

[19] T. Alammar, I. Hamm, M. Wark, A. Mudring, Low-temperature route to metal titanate perovskite nanoparticles for photocatalytic applications, Appl Catal B: Environ. (2014).

[20] A. Chongterdtoonskul, J.W. Schwank, S. Chavadej, Ethylene Epoxidation Activity Over Ag-Based Catalysts on Different Nanocrystalline Perovskite Titanate Supports, Catal Lett. 142 (2012) 991-1002.

[21] J. Moreno, J.M. Dominguez, A. Montoya, L. Vicente, T. Viveros, Synthesis and characterization of $MTiO_3$ (M= Mg, Ca, Sr, Ba) sol-gel, J Mater Chem. 5 (1995) 509-512.

[22] W.W. Lee, W. Chung, W. Huang, W. Lin, W. Lin, Y. Jiang, C. Chen, Photocatalytic activity and mechanism of nano-cubic barium titanate prepared by a hydrothermal method, J Taiwan Inst Chem Eng. 44 (2013) 660-669.

[23] S. Song, L. Xu, Z. He, H. Ying, J. Chen, X. Xiao, B. Yan, Photocatalytic degradation of CI Direct Red 23 in aqueous solutions under UV irradiation using $SrTiO_3/CeO_2$ composite as the catalyst, J Hazard Mater. 152 (2008) 1301-1308.

[24] D.S. Bhatkhande, V.G. Pangarkar, A.A. Beenackers, Photocatalytic degradation for environmental applications–a review, J Chem Tech Biotech. 77 (2002) 102-116.

[25] K. Maeda, T. Takata, M. Hara, N. Saito, Y. Inoue, H. Kobayashi, K. Domen, GaN: ZnO solid solution as a photocatalyst for visible-light-driven overall water splitting, J Am Chem Soc. 127 (2005) 8286-8287.

[26] J.S. Lee, Photocatalytic water splitting under visible light with particulate semiconductor catalysts, Catal Surv Asia. 9 (2005) 217-227.

[27] H. Frederikse, W. Thurber, W. Hosler, Electronic transport in strontium titanate, Phys Rev. 134 (1964) A442.

[28] X. Yan, S. Sun, B. Hu, X. Wang, W. Lu, W. Shi, Enhanced photocatalytic activity induced by surface plasmon resonance on Ag-loaded strontium titanate nanoparticles, Micro Nano Lett, IET. 8 (2013) 504-507.

[29] P. Shen, J.C. Lofaro Jr., W.R. Woerner, M.G. White, D. Su, A. Orlov, Photocatalytic activity of hydrogen evolution over Rh doped $SrTiO_3$ prepared by polymerizable complex method, Chem Eng J. 223 (2013) 200-208.

[30] T.K. Townsend, N.D. Browning, F.E. Osterloh, Nanoscale strontium titanate photocatalysts for overall water splitting, ACS Nano. 6 (2012) 7420-7426.

[31] T. Puangpetch, S. Chavadej, T. Sreethawong, Hydrogen production over Au-loaded mesoporous-assembled $SrTiO_3$ nanocrystal photocatalyst: effects of molecular structure and chemical properties of hole scavengers, Energ Conv Manag. 52 (2011) 2256-2261.

[32] J. Jang, J.S. Lee, P.H. Borse, K. Lim, O. Jung, E. Jeong, M. Won, H. Kim, Platinum Nanoparticle Co-Catalyst-Induced Improved Photoelectrical Properties in a Chromium-Doped $SrTiO_3$ Photocatalyst, J Korean Phys Soc. 55 (2009) 2470-2475.

[33] J. Wang, Y. Ling, X. Lu, H. Wang, F. Qian, Y. Tongb, Y. Li, Photochemical charge transfer observed in nanoscale hydrogen evolving photocatalysts using surface photovoltage spectroscopy, Nanoscale. 8 (2015) 2970.

[34] D. Bui, J. Mu, L. Wang, S. Kang, X. Li, Preparation of Cu-loaded $SrTiO_3$ nanoparticles and their photocatalytic activity for hydrogen evolution from methanol aqueous solution, Appl Surf Sci 274 (2013) 328-333.

[35] A.J. Haes, R.P. Van Duyne, A unified view of propagating and localized surface plasmon resonance biosensors, Anal Bioanal Chem. 379 (2004) 920-930.

[36] T.R. Jensen, M.D. Malinsky, C.L. Haynes, R.P. Van Duyne, Nanosphere lithography: tunable localized surface plasmon resonance spectra of silver nanoparticles, J Phys Chem B. 104 (2000) 10549-10556.

[37] X. Chen, Z. Zheng, X. Ke, E. Jaatinen, T. Xie, D. Wang, C. Guo, J. Zhao, H. Zhu, Supported silver nanoparticles as photocatalysts under ultraviolet and visible light irradiation, Green Chem. 12 (2010) 414-419.

[38] E. Stathatos, P. Lianos, P. Falaras, A. Siokou, Photocatalytically deposited silver nanoparticles on mesoporous TiO_2 films, Langmuir. 16 (2000) 2398-2400.

[39] E. Albiter, M.A. Valenzuela, S. Alfaro, G. Valverde-Aguilar, F.M. Martínez-Pallares, Photocatalytic deposition of Ag nanoparticles on TiO_2: Metal precursor effect on the structural and photoactivity properties, J Saudi Chem Soc. 19 (2015) 563-573.

[40] J. Liu, Y. Sun, Z. Li, S. Li, J. Zhao, Photocatalytic hydrogen production from water/methanol solutions over highly ordered Ag–$SrTiO_3$ nanotube arrays, Int J Hydrogen Energ. 36 (2011) 5811-5816.

[41] H. Tada, K. Teranishi, S. Ito, Additive effect of sacrificial electron donors on Ag/TiO_2 photocatalytic reduction of bis (2-dipyridyl) disulfide to 2-mercaptopyridine in aqueous media, Langmuir. 15 (1999) 7084-7087.

[42] K. Patel, S. Kapoor, D. Dave, T. Mukherjee, Synthesis of nanosized silver colloids by microwave dielectric heating, J Chem Sci. 117 (2005) 53-60.

[43] A. Sclafani, M. Mozzanega, J. Herrmann, Influence of silver deposits on the photocatalytic activity of titania, J Catal. 168 (1997) 117-120.

[44] G.W. Busser, B. Mei, M. Muhler, Optimizing the Deposition of Hydrogen Evolution Sites on Suspended Semiconductor Particles using On-Line Photocatalytic Reforming of Aqueous Methanol Solutions, ChemSusChem. 5 (2012) 2200-2206.

[45] W. Wei, Y. Dai, M. Guo, Y. Zhu, B. Huang, Density functional theory study of Ag adsorption on $SrTiO_3$ (001) surface, J Phys Chem C. 114 (2010) 10917-10921.

[46] A.J. Bard, M.A. Fox, Artificial photosynthesis: solar splitting of water to hydrogen and oxygen, Acc Chem Res. 28 (1995) 141-145.

[47] P. Rao, M. Ansari, A. Gavane, V. Pandit, P. Nema, S. Devotta, Seasonal variation of toxic benzene emissions in petroleum refinery, Environ Monit Assess. 128 (2007) 323-328.

[48] M. Kampa, E. Castanas, Human health effects of air pollution, Environ Pollut. 151 (2008) 362-367.

[49] P. Jaramillo, W.M. Griffin, H.S. Matthews, Comparative life-cycle air emissions of coal, domestic natural gas, LNG, and SNG for electricity generation, Environ Sci Technol. 41 (2007) 6290-6296.

[50] R.K. Srivastava, N. Hutson, B. Martin, F. Princiotta, J. Staudt, Control of mercury emissions from coal-fired electric utility boilers, Environ Sci Technol. 40 (2006) 1385-1393.

[51] S. Shafiee, E. Topal, When will fossil fuel reserves be diminished? Energ Policy. 37 (2009) 181-189.

[52] A. Demirbas, Potential applications of renewable energy sources, biomass combustion problems in boiler power systems and combustion related environmental issues, Prog Energ Combus. 31 (2005) 171-192.

[53] T. Searchinger, R. Heimlich, R.A. Houghton, F. Dong, A. Elobeid, J. Fabiosa, S. Tokgoz, D. Hayes, T.H. Yu, Use of U.S. croplands for biofuels increases greenhouse gases through emissions from land-use change, Science. 319 (2008) 1238-1240.

[54] D. Pimentel, Ethanol fuels: energy balance, economics, and environmental impacts are negative, Nat Resour Res. 12 (2003) 127-134.

[55] D. Pimentel, A. Marklein, M.A. Toth, M. Karpoff, G.S. Paul, R. McCormack, J. Kyriazis, T. Krueger, Biofuel impacts on world food supply: use of fossil fuel, land and water resources, Energies. 1 (2008) 41-78.

[56] C. Koroneos, A. Dompros, G. Roumbas, N. Moussiopoulos, Life cycle assessment of hydrogen fuel production processes, Int J Hydrogen Energ. 29 (2004) 1443-1450.

[57] P.C. Hallenbeck, J.R. Benemann, Biological hydrogen production; fundamentals and limiting processes, Int J Hydrogen Energ. 27 (2002) 1185-1193.

[58] S.H. Jensen, X. Sun, S.D. Ebbesen, R. Knibbe, M. Mogensen, Hydrogen and synthetic fuel production using pressurized solid oxide electrolysis cells, Int J Hydrogen Energ. 35 (2010) 9544-9549.

[59] G. Kortüm, W. Braun, G. Herzog, Principles and Techniques of Diffuse-Reflectance Spectroscopy, Angew Chem Int Edit. 2 (1963) 333-341.

[60] S. Taylor, M. Mehta, A. Samokhvalov, Production of Hydrogen by Glycerol Photoreforming Using Binary Nitrogen–Metal-Promoted N-M-TiO_2 Photocatalysts, ChemPhysChem. 15 (2014) 942-949.

[61] R.P. Antony, T. Mathews, C. Ramesh, N. Murugesan, A. Dasgupta, S. Dhara, S. Dash, A. Tyagi, Efficient photocatalytic hydrogen generation by Pt modified TiO_2 nanotubes fabricated by rapid breakdown anodization, Int J Hydrogen Energ. 37 (2012) 8268-8276.

[62] X. Wu, D. Wu, X. Liu, Negative pressure effects in $SrTiO_3$ nanoparticles investigated by Raman spectroscopy, Solid State Commun. 145 (2008) 255-258.

[63] A. Souza, G. Santos, B. Barra, W. Macedo Jr, S. Teixeira, C. Santos, A. Senos, L. Amaral, E. Longo, Photoluminescence of $SrTiO_3$: influence of particle size and morphology, Cryst Growth Des. 12 (2012) 5671-5679.

[64] R. Durman, P. Favre, U. Jayasooriya, S. Kettle, Longitudinal optical-transverse optical (LO-TO) splitting on internal modes in the Raman spectra of noncentric crystals, J Cryst Spectrosc. 17 (1987) 431-484.

[65] J.B. Goodall, S. Kellici, D. Illsley, R. Lines, J.C. Knowles, J.A. Darr, Optical and photocatalytic behaviours of nanoparticles in the Ti–Zn–O binary system, RSC Adv. 4 (2014) 31799-31809.

[66] D. Wood, J. Tauc, Weak absorption tails in amorphous semiconductors, Phys Rev B. 5 (1972) 3144.

[67] W. Zhang, Z. Yin, M. Zhang, Z. Du, W. Chen, Roles of defects and grain sizes in photoluminescence of nanocrystalline $SrTiO_3$, J Phys: Condens Mat. 11 (1999) 5655.

[68] W. Zhang, Z. Yin, M. Zhang, Study of photoluminescence and electronic states in nanophase strontium titanate, Appl Phys A. 70 (2000) 93-96.

[69] C. Pinheiro, E. Longo, E. Leite, F. Pontes, R. Magnani, J.A. Varela, P. Pizanni, T. Boschi, F. Lanciotti, The role of defect states in the creation of photoluminescence in $SrTiO_3$, Appl Phys A. 77 (2003) 81-85.